Nodal arrangement of HOMO controls the turning ON/OFF the electronic coupling in isomeric polypyrene wires

Maxim V. Ivanov, Khushabu Thakur, Anitha Boddeda, Denan Wang, and Rajendra Rathore

Department of Chemistry, Marquette University, P.O. Box 1881, Milwaukee, WI 53201-1881

Supporting Information

Table of content

Experiment

S1. Synthesis

Synthesis of m-Py$_n$

Scheme S1: Synthesis of Pyrene1

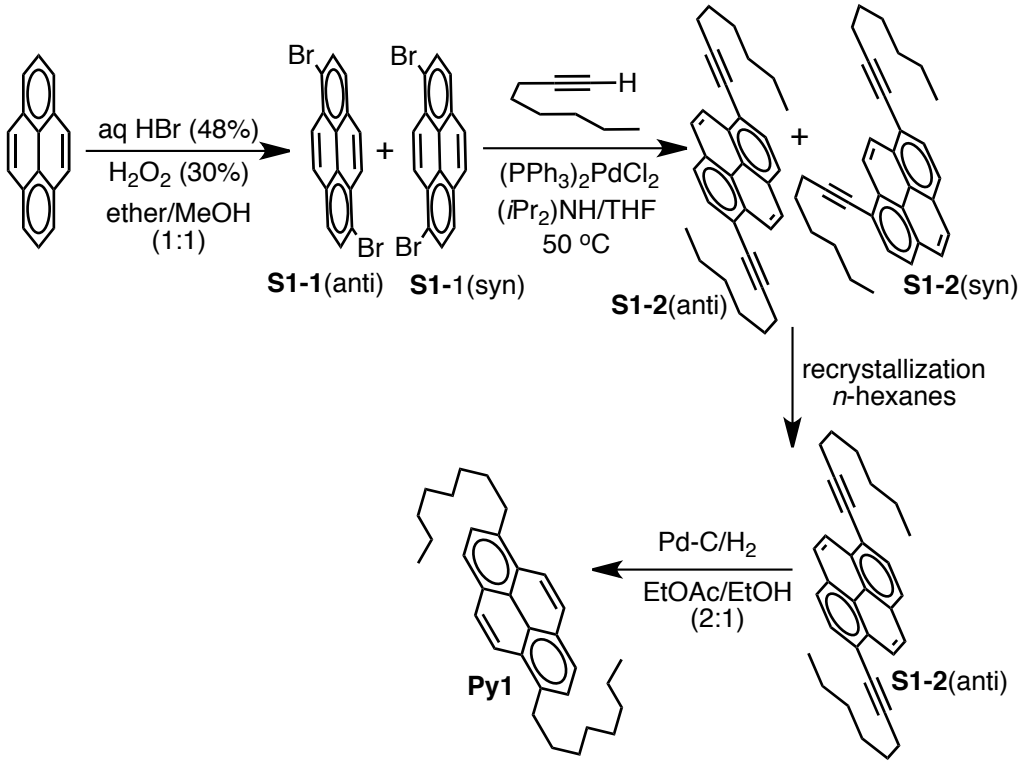

Synthesis of S1-1.

The isomeric mixture of dibromopyrenes was prepared by following a procedure detailed below. The aqueous HBr (48%, 14.8 mL) was added to a solution of pyrene (12.0 g, 59.33 mmol) in ether (150 mL) and methanol (150 mL) under argon atmosphere. To the resulting mixture, 30% aqueous solution of H_2O_2 (12.2 mL) was added dropwise over 20 min and it was allowed to stir at 22^0C for 24 hrs. After 24 hrs of stirring a voluminous precipitate was formed. The precipitate was filtered and washed with hot ethanol (2 × 30 mL). Product was dried under vacuum (8.0 g, 74%), m.p: 120-122^0C. ^{1}H NMR ($CDCl_3$, 400 MHz) δ: 8.03-8.08 (3H, m), 8.09-8.15 (1H, d, J = 9.26 Hz), 8.24-8.30 (2H, dd, J = 8.20 Hz), 8.43, 8.49 (1H, d, J = 9.24 Hz), 8.52-8.56 (1H, s). ^{13}C NMR ($CDCl_3$, 400 MHz) δ: 120.6, 120.89, 125.25, 125.28, 126.06, 126.28, 126.37, 127.50, 127.58, 128.74, 129.56, 129.74, 130.48, 130.67, 130.76, 130.81.

Synthesis of S1-2.

To the mixture of dibromopyrene (S1-1) (6.0 g, 16.66 mmol) in dry THF (40 mL), $PdCl_2(PPh_3)_2$ (80 mg) and 1-Octyne (5.50 g, 49.98 mmol) in $NH(iPr)_2$ (40 mL) and CuI (120 mg) were added in an oven dried Schlenk flask under argon atmosphere. The resulting mixture was stirred at 50^0C for 12 hours. The resulting mixture was cooled to room temperature, and insoluble materials were removed by filtration and filtrate was washed with water and extracted with dichloromethane (3 x 30 mL). The combined organic layers were dried over anhydrous magnesium sulfate, evaporated and dried under vacuum. The resulting crude product was purified by flash column to afford mixture of cis and trans isomers (S1-2). And these cis and trans isomers were further separated by multiple crystallizations from Hexane to afford pure S1-3. Trans: ^{1}H NMR ($CDCl_3$, 400 MHz) δ: 0.95 (6H, m), 1.40 (8H, m), 1.60 (4H, m), 1.74 (4H, m), 2.65 (4H, t, J = 7.05Hz), 8.00 (2H, s), 8.06 (4H, s), 8.62 (2H, s). Cis: ^{1}H NMR ($CDCl_3$, 400 MHz) δ: 0.95 (6H, m), 1.40 (8H, m), 1.60 (4H, m), 1.77 (4H, m), 2.65 (4H, t, J = 7.05 Hz), 8.04-8.11 (6H, s), 8.55 (2H, d, J = 9.29 Hz).

Synthesis of Py1.

The S1-3 (2.0 g) from above was placed into a Parr apparatus along with a stir bar and dissolved in Ethyl acetate / Ethanol (20:5 mL). To the solution, 10% Palladium on activated Carbon catalyst (100 mg) was added. The vessel was then put under hydrogen pressure (3 bar) for 2 hours after which time the solution was filtered over a short pad of silica gel. The silica gel was washed with ethyl acetate (2 x 30 mL), the solvent was evaporated and the resulting 1,8-dioctane pyrene was dried under vacuum to afford crude product which was purified by column chromatography using hexane as a solvent. (2.0 g, 98%), m.p: 92-93^{0}C. ^{1}H NMR ($CDCl_3$, 400 MHz) δ: 0.88 (6H, m), 1.22-1.42 (16H, m), 1.47 (4H, m), 1.84 (4H, m), 3.32 (4H, m), 7.84 (2H, d, J = 7.82 Hz), 8.05 (2H, d, J = 9.32 Hz), 8.08 (2H, d, J = 7.82 Hz), 8.21 (2H, d, J = 9.32 Hz). ^{13}C NMR ($CDCl_3$, 400 MHz) δ: 14.29, 22.84, 29.49, 29.74, 30.02, 32.07, 33.90, 122.69, 124.53, 127.31, 127.35, 128.99, 129.61, 137.18.

Scheme S2: Synthesis of Py2

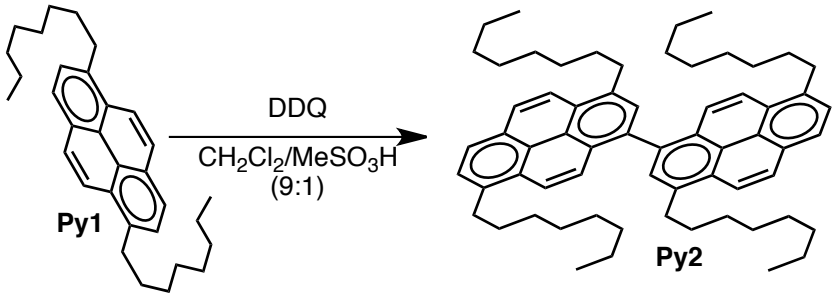

To the solution of Pyrene1 (0.1 g, 0.234 mmol) in anhydrous DCM (9 mL) was added methane sulfonic acid (1 mL) in an oven dried Schlenk flask under argon atmosphere. Upon stirring color of the solution changed from red to purple to green. To the stirring solution was added DDQ (0.03 g, 0.12 mmol) and reaction mixture was stirred for another 30 minutes. The resulting reaction mixture

was quenched by pouring onto saturated aqueous $NaHCO_3$ (20 mL). The organic layer was separated and the aqueous layer was extracted with dichloromethane (3 x 20 mL). The combined organic layers were washed with water and brine, dried over anhydrous $MgSO_4$, filtered and evaporated under vacuum to afford crude Pyrene2 which was purified by column chromatography using hexane as a solvent (0.05 g, 49%), m.p: 110-111^{0}C. ^{1}H NMR ($CDCl_3$, 400 MHz) δ: 0.79- 0.92 (12H, m), 1.17- 1.55 (40H, m), 1.72- 1.83 (4H, m), 1.89- 1.99 (4H, m), 3.20- 3.28 (4H, m), 3.38- 3.45 (4H, m), 7.68 (2H, d, J = 9.58 Hz), 7.86 (2H, d, J = 7.81 Hz), 7.99- 8.03 (4H, m), 8.14 (4H, d, J = 8.91 Hz), 8.35 (2H, d, J = 9.29 Hz). ^{13}C NMR ($CDCl_3$, 400 MHz) δ: 14.24, 14.29, 22.79, 22.85, 29.44, 29.54, 29.73, 29.96, 30.08, 32.01, 32.05, 33.85, 122.77, 122.83, 124.82, 125.81, 125.87, 127.49, 128.60, 128.78, 128.86, 129.97, 130.30, 136.00, 136.53, 137.27.

Scheme S3: Synthesis of Py3

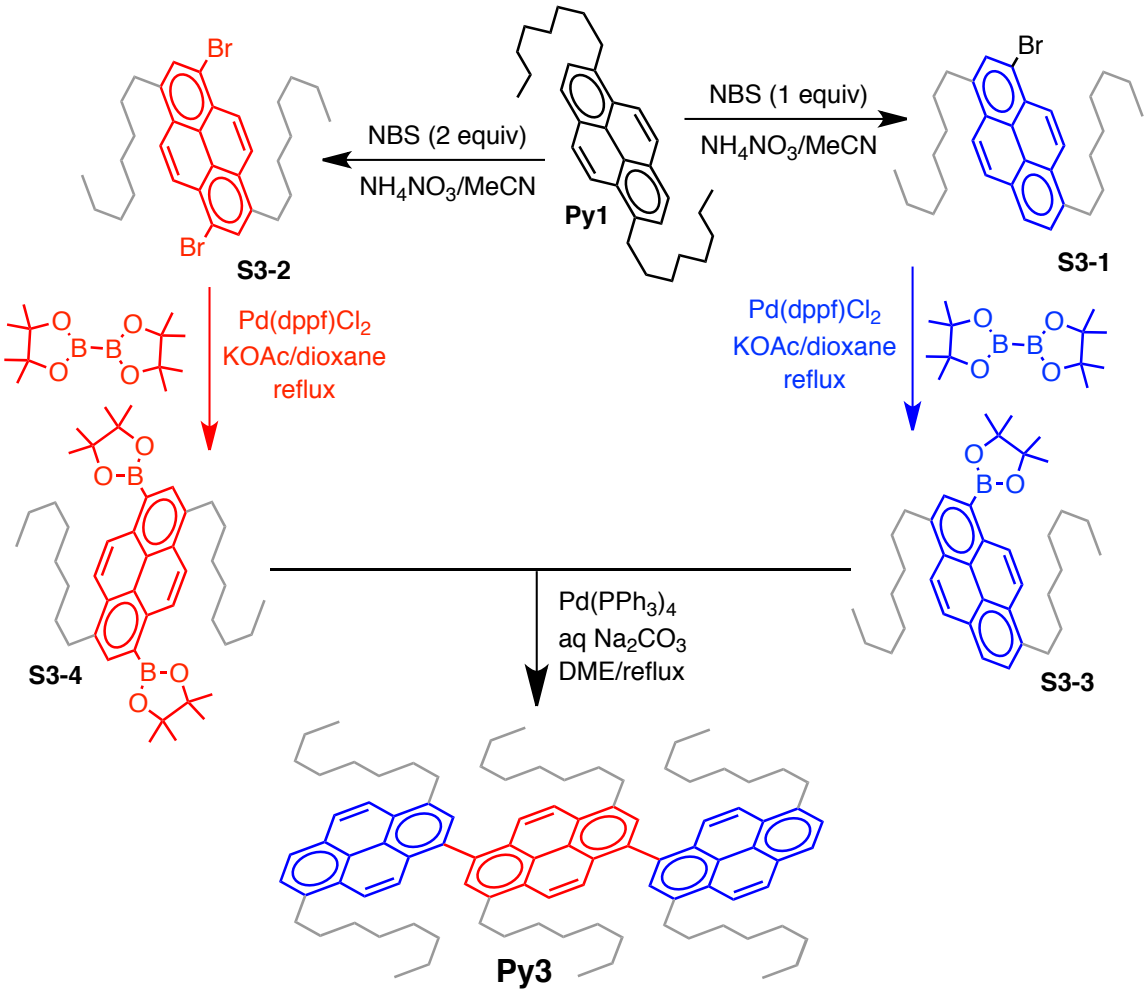

Synthesis of S3-1.

To the solution of 1,8-dioctylpyrene (Pyrene1) (0.6 g, 1.4 mmol) in $CHCl_3$ (40 mL) was added NBS (0.25 g, 1.4 mmol) and NH_4NO_3 (0.011 g, 0.14 mmol) in oven dried Schlenk flask under argon

atmosphere and the resulting reaction mixture was allowed to stir at room temperature for overnight. Then the reaction mixture quenched with water (30 mL) and extracted with DCM (3 x 25 mL). The combined organic layers were dried over $MgSO_4$, filtered and evaporated under reduced pressure to give (S3-1) (0.6 g, 84.5%). ^{1}H NMR ($CDCl_3$, 400 MHz) δ: 0.87 (6H, m), 1.16-1.56 (20H, m), 1.83 (4H, m), 3.29 (4H, m), 7.83 (1H, d, J = 7.76 Hz), 8.01-8.14 (3H, m), 8.17-8.27 (2H, m), 8.44 (1H, d, J = 9.44 Hz).

Synthesis of S3-2.

To the solution of pyrene1 (0.3 g, 0.703 mmol) in $CHCl_3$ (40 mL) was added NBS (0.25 g, 1.4 mmol) and NH_4NO_3 (0.011 g, 0.14 mmol) in oven dried Schlenk flask under argon atmosphere and the reaction mixture was allowed to stir at room temperature for overnight. Then the reaction was quenched by addition of water (30 ml) and it was extracted with DCM (3 x 20 mL). The combined organic layers were dried over $MgSO_4$, filtered and evaporated under reduced pressure to give S3-2 (0.3g, 73%), m.p: 98-100^{0}C. ^{1}H NMR ($CDCl_3$, 400 MHz) δ: 0.88 (6H, m), 1.19-1.53 (20H, m), 1.82 (4H, m), 3.27 (4H, m), 8.12 (2H, s), 8.23 (2H, d, J = 9.54 Hz), 8.42 (2H, d, J = 9.54 Hz).^{13}C NMR ($CDCl_3$, 400 MHz) δ: 14.29, 22.84, 29.49, 29.74, 30.02, 32.07, 33.91, 122.70, 124.54, 127.32, 127.35, 128.99, 129.61, 137.19.

Synthesis of S3-3.

To an oven dried Schlenk flask under argon atmosphere, mixture of S1-1 (0.70 g, 1.38 mmol), Pd(dppf)Cl_2 (50 mg) in 1,4-Dioxane (30 mL), potassium acetate (0.34 g, 3.46 mmol) and bis(pinacolato)diboron (0.70 g, 2.77 mmol) were added and the resulting reaction mixture was allowed to reflux overnight. Then the reaction was quenched by addition of water (30 mL). It was then extracted with DCM (3 x 25 mL), dried over $MgSO_4$, filtered and evaporated under vacuum to yield crude product. It was then subjected to column chromatography with hexane as solvent to give pure product S3-3 (0.6 g, 78%), m.p: 78-80^{0}C. ^{1}H NMR ($CDCl_3$, 400 MHz) δ: 0.89 (6H, m), 1.20-1.43 (20H, m), 1.49 (12H, m), 1.84 (4H, m), 3.32 (4H, m), 7.84 (1H, d, J = 7.74 Hz), 8.06 (2H, t, J = 10.09 Hz), 8.21 (1H, d, J = 9.26Hz), 8.30 (1H, d, J = 9.26 Hz), 8.35 (1H, s), 9.11 (1H, d, J = 7.51 Hz). ^{13}C NMR ($CDCl_3$, 400 MHz) δ: 14.35, 22.91, 25.26, 29.56, 29.58, 29.80, 29.81, 30.13, 30.29, 32.14, 32.31, 32.37, 34.09, 34.11, 83.45, 122.77, 123.19, 124.87, 125.48, 125.64, 127.22, 127.92, 128.64, 128.68, 129.61, 131.50, 135.04, 135.35, 136.05, 137.74.

Synthesis of S3-4.

To an oven dried Schlenk flask under argon atmosphere, mixture of S1-2 (0.50 g, 0.86 mmol), Pd(dppf)Cl_2 (50 mg) in 1,4-Dioxane (30 mL), potassium acetate (0.25 g, 2.58 mmol) and bis(pinacolato)diboron (0.48 g, 1.90 mmol) were added and the resulting reaction mixture was allowed to reflux overnight. And the reaction was quenched by addition of water (30 mL). It was then extracted with DCM (3 x 20 mL), dried over $MgSO_4$, filtered and evaporated under vacuum to yield crude product. It was then purified by column chromatography with hexane/ethyl acetate mixture as

a solvent to give pure product S1-4 (0.36 g, 63%), m.p: 126-128^{0}C. ^{1}H NMR ($CDCl_3$, 400 MHz) δ: 0.88 (6H, m), 1.18-1.42 (20H, m), 1.48 (24H, m), 1.84 (4H, m), 3.32 (4H, m), 8.30 (2H, d, J = 9.5 Hz), 8.35 (2H, s), 9.11 (2H, d, J = 9.5 Hz). ^{13}C NMR ($CDCl_3$, 400 MHz) δ: 14.30, 22.85, 25.18, 29.53, 29.75, 30.29, 32.08, 32.49, 34.17, 83.91, 123.18, 125.39, 129.01, 130.99, 134.87, 135.11, 136.49.

The S3-4 (0.6 g, 0.884 mmol) and S3-1 (1.0 g, 1.94 mmol) were dissolved in anhydrous 1,2-dimethoxyethane (DME) (60 mL) in an oven dried Schlenk flask under an argon atmosphere and the flask was evacuated and filled with argon (3x). In another oven dried Schlenk flask a solution of anhydrous sodium carbonate (5.0 g) in water (20 mL) was prepared under an argon atmosphere and the flask was also evacuated and filled with argon (3x). To the DME solution, $Pd(PPh_3)_4$ (50 mg) and the salt solution were added sequentially under a strict argon atmosphere followed by evacuation and filling the flask with argon (3x) after each addition. The flask was covered with foil and the solution was allowed to reflux overnight. The resulting solution was cooled to room temperature, quenched with water (50 mL) and extracted with dichloromethane (3 x 25 mL). The organic layer was dried over anhydrous magnesium sulfate, evaporated and dried under vacuum to afford crude product. The crude product was purified by column chromatography using a hexanes/ethyl acetate mixture to give the pure Pyrene3 (0.45g, 40%), m.p: 146-148^{0}C. ^{1}H NMR ($CDCl_3$, 400 MHz) δ: 0.77-0.92 (18H, m), 1.14-1.60 (60H, m), 1.75-2.03 (12H, m), 3.21-3.50 (12H, m), 7.70-7.80 (4H, m), 7.88 (2H, d), 8.02 (2H, s), 8.04-8.87 (4H, m), 8.13-8.19 (6H, m), 8.37 (2H, d). ^{13}C NMR ($CDCl_3$, 400 MHz) δ: 14.23, 14.25, 14.30, 22.79, 22.80, 22,87, 29.47, 29.48, 29.56, 29.65, 29.69, 29.76, 29.98, 30.02, 30.11, 31.98, 32.03, 32.07, 33.87, 33.90, 34.01, 122.80, 122.87, 124.86, 125.84, 125.91, 125.93, 126.04, 127.53, 128.63, 128.65, 128.82, 128.88, 128.95, 129.99, 130.33, 130.49, 136.10, 136.24, 136.27, 136.56, 136.60, 136.62, 137.31.

Scheme S5: Synthesis of Py4

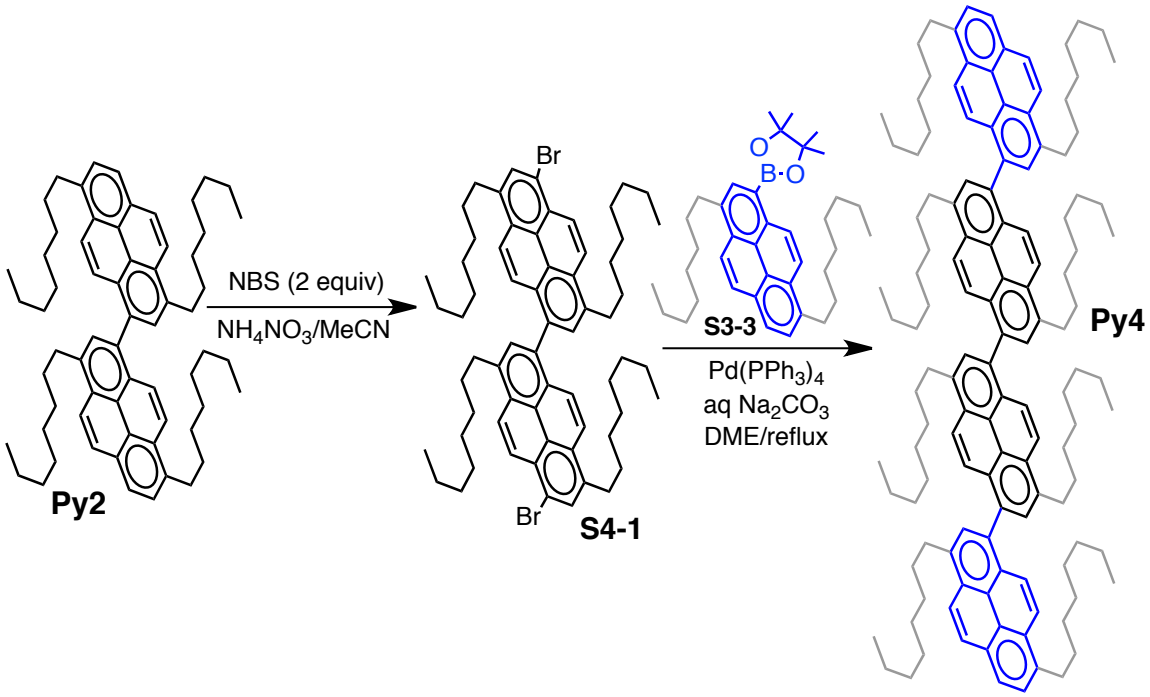

Synthesis of S5-1.

To the solution of pyrene2 (0.2 g, 0.24 mmol) in $CHCl_3$ (20 mL) was added NBS (0.08 g, 0.48 mmol) and NH_4NO_3 (0.02 g, 0.02 mmol) under argon and the resulting reaction mixture was allowed to stir at room temperature for overnight. Then the reaction was quenched by addition of water (30 mL) and it was extracted with DCM (3 x 20 mL). The combined organic layers were dried over $MgSO_4$, filtered and evaporated under reduced pressure to give crude product which was further purified by column chromatography using hexane and ethyl acetate mixture as eluent to afford pure S5-1 (0.15 g, 63%), m.p: 134-135^{0}C. ^{1}H NMR ($CDCl_3$, 400 MHz) δ: 0.76-0.90 (12H, m), 1.14-1.55 (40H, m), 1.70-1.81 (4H, m), 1.87-1.98 (4H, m), 3.15-3.22 (4H, m), 3.37-3.45 (4H, m), 7.65 (2H, d, J = 9.53 Hz), 7.96 (2H, d, J = 9.53 Hz), 8.00 (2H, s), 8.12 (2H, s), 8.44 (2H, d, J = 9.53 Hz), 8.52 (2H, d, J = 9.53 Hz). ^{13}C NMR ($CDCl_3$, 400 MHz) δ: 14.25, 14.29, 22.79, 22.85, 29.40, 29.53, 29.61, 29.71, 29.89, 30.06, 31.74, 31.99. 32.04, 32.09, 33.49, 33.92, 119.92, 122.65, 124.28, 125.29, 126.02, 127.06, 128.32, 128.44, 128.66, 128.69, 130.82, 131.35, 136.48, 137.20, 138.13.

Synthesis of Py4.

The S5-1 (0.35 g, 0.24 mmol) and S3-3 (0.34 g, 0.61 mmol) were dissolved in anhydrous 1,2-dimethoxyethane (DME) (60 mL) in an oven dried Schlenk flask under an argon atmosphere and the flask was evacuated and filled with argon (3x). In another oven dried Schlenk flask a solution of anhydrous sodium carbonate (5.0 g) in water (20 mL) was prepared under an argon atmosphere and the flask was also evacuated and filled with argon (3x). To the DME solution, $Pd(PPh_3)_4$ (50 mg) and the salt solution were added sequentially under a strict argon atmosphere followed by evacuation

and filling the flask with argon (3x) after each addition. The flask was covered with foil and the solution was allowed to reflux overnight. The resulting solution was cooled to room temperature, quenched with water (50 mL) and extracted with dichloromethane (3 x 25 mL). The organic layer was dried over anhydrous magnesium sulfate, evaporated and dried under vacuum. The crude product was purified by column chromatography using a hexanes/ethyl acetate mixture to give the pure Pyrene4 (0.2 g, 40%), m.p: 162-164^{0}C. ^{1}H NMR ($CDCl_3$, 400 MHz) δ: 0.77-0.94 (24H, m), 1.16-1.61 (80H, m), 1.74-2.06 (16H, m), 3.23-3.51 (16H, m), 7.70-7.92 (8H, m), 8.01-8.10 (8H, m), 8.14-8.21 (8H, m), 8.37 (2H, d). ^{13}C NMR ($CDCl_3$, 400 MHz) δ: 14.25, 14.30, 22.80, 22,87, 29.49, 29.56, 29.67, 29.76, 29.99, 30.04, 30.11, 32.00, 32.03, 32.07, 33.93, 34.01, 122.82, 124.87, 125.84, 125.91, 125.95, 126.05, 127.54, 128.65, 128.82, 128.89, 128.97, 128.98, 130.00, 130.34, 130.51, 136.10, 136.27, 136.30, 136.33, 136.35, 136.40, 136.58, 136.61, 136.65, 137.33.

Scheme S6: Synthesis of Py5

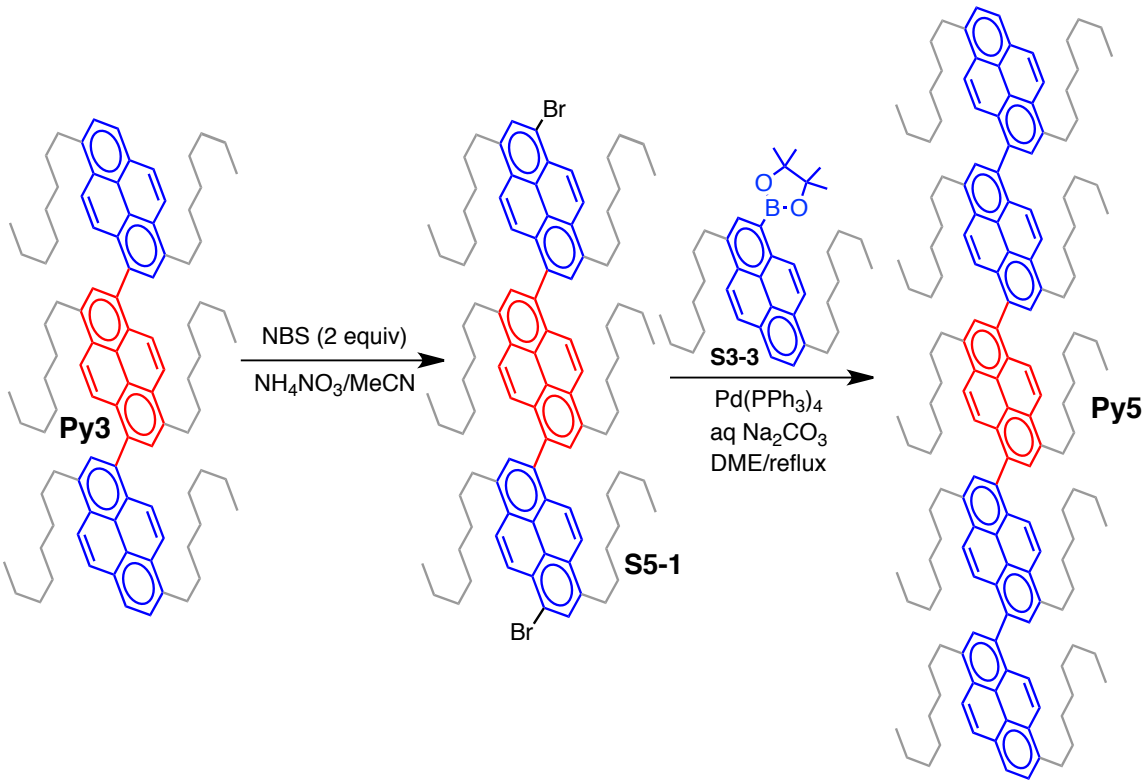

Synthesis of S6-1.

To the solution of pyrene3 (0.25 g, 0.2 mmol) in $CHCl_3$ (30 mL) was added NBS (0.07 g, 0.4 mmol) and NH_4NO_3 (0.02 g, 0.02 mmol) under argon and the resulting reaction mixture was allowed to stir at room temperature for overnight. Then the reaction was quenched by addition of water (30 mL) and it was extracted with DCM (3 x 20 mL). The combined organic layers were dried over $MgSO_4$, filtered and evaporated under reduced pressure to give crude product which was further purified by

column chromatography using hexane and ethyl acetate mixture as eluent to afford pure S5-1 (0.35 g, 77%). ^{1}H NMR ($CDCl_3$, 400 MHz) δ: 0.72-0.94 (18H, m), 1.10-1.60 (60H, m), 1.70-2.03 (12H, m), 3.14-3.51 (12H, m), 7.73 (4H, d), 7.95-8.17 (10H, m), 8.43-8.57 (4H, m). ^{13}C NMR ($CDCl_3$, 400 MHz) δ: 14.25, 14.31, 22.80, 22.87, 29.43, 29.48, 29.55, 29.65, 29.75, 29.93, 30.03, 30.09, 31.78, 31.99, 32.02, 32.07, 32.15, 33.56, 33.90, 33.98, 119.90, 122.62, 122.65, 123.00, 124.37, 125.38, 125.89, 126.00, 126.03, 126.13, 126.14, 126.16, 127.18, 128.40, 128.55, 128.67, 128.70, 128.81, 128.93, 130.47, 130.95, 131.39, 136.01, 136.73, 136.92, 137.25, 137.30, 138.13, 138.14.

Synthesis of Py5

The S6-1 (0.3 g, 0.3 mmol) and S3-3 (0.41 g, 0.74 mmol) were dissolved in anhydrous 1,2-dimethoxyethane (DME) (60 mL) in an oven dried Schlenk flask under an argon atmosphere and the flask was evacuated and filled with argon (3x). In another oven dried Schlenk flask a solution of anhydrous sodium carbonate (5.0 g) in water (20 mL) was prepared under an argon atmosphere and the flask was also evacuated and filled with argon (3x). To the DME solution, $Pd(PPh_3)_4$ (50 mg) and the salt solution were added sequentially under a strict argon atmosphere followed by evacuation and filling the flask with argon (3x) after each addition. The flask was covered with foil and the solution was allowed to reflux overnight. The resulting solution was cooled to room temperature, quenched with water (50 mL) and extracted with dichloromethane (3 x 25 mL). The organic layer was dried over anhydrous magnesium sulfate, evaporated and dried under vacuum. The crude product was purified by column chromatography using a hexanes/ethyl acetate mixture to give the pure Pyrene5 (0.09 g, 30%), m.p: 198-200^{0}C. ^{1}H NMR ($CDCl_3$, 400 MHz) δ: 0.73-0.94 (30H, m), 1.09-1.61 (100H, m), 1.70-2.07 (20H, m), 3.19-3.53 (20H, m), 7.68-7.78 (4H, m), 7.84-7.91 (4H, m), 7.99-8.20 (20H, m), 8.33-8.41 (4H, m). ^{13}C NMR ($CDCl_3$, 400 MHz) δ: 14.25, 14.30, 22.81, 22.87, 29.51, 29.56, 29.69, 29.76, 30.00, 30.06, 30.12, 32.01, 32.07, 33.96, 122.83, 122.85, 122.89, 122.90, 122.92, 122.94, 124.88,125.85,125.91, 125.97,125.98, 126.02, 126.07, 127.55, 128.66, 128.83, 128.90, 128.97, 129.01, 130.01, 130.36, 130.52, 136.11, 136.36 (broad), 136.60, 136.63, 136.63, 136.67, 136.69, 136.70, 137.35.

NMR Spectroscopy

^{1}H NMR spectrum of S1-1(anti) and S1-1(syn) in $CDCl_3$

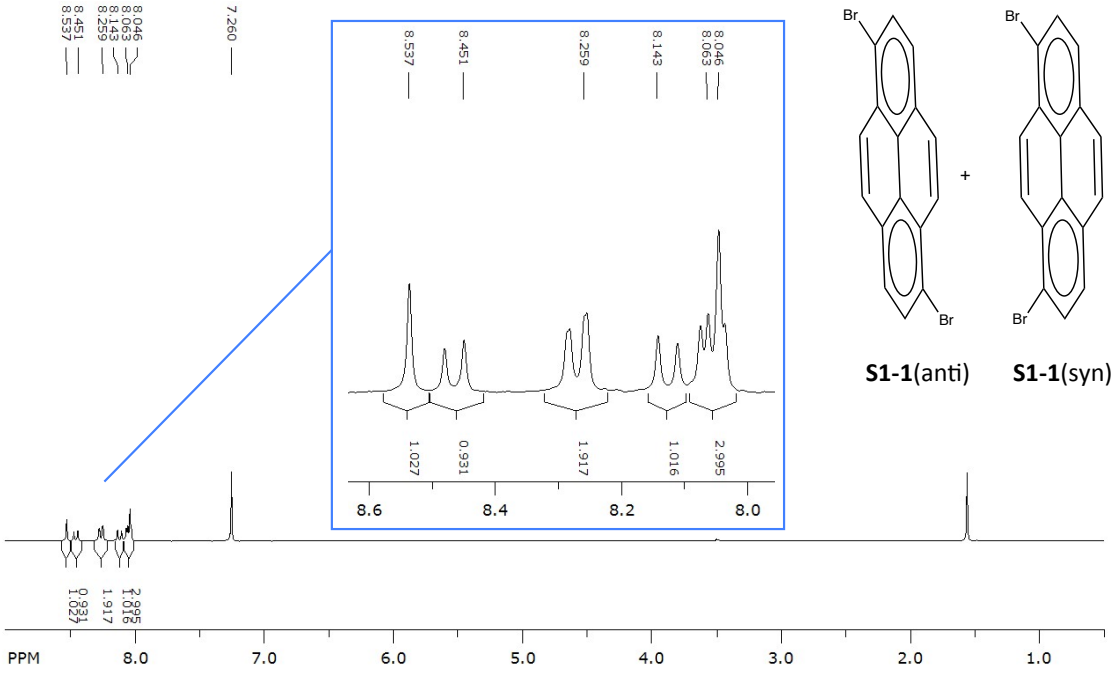

^{13}C NMR spectrum of S1-1(anti) and S1-1(syn) in $CDCl_3$

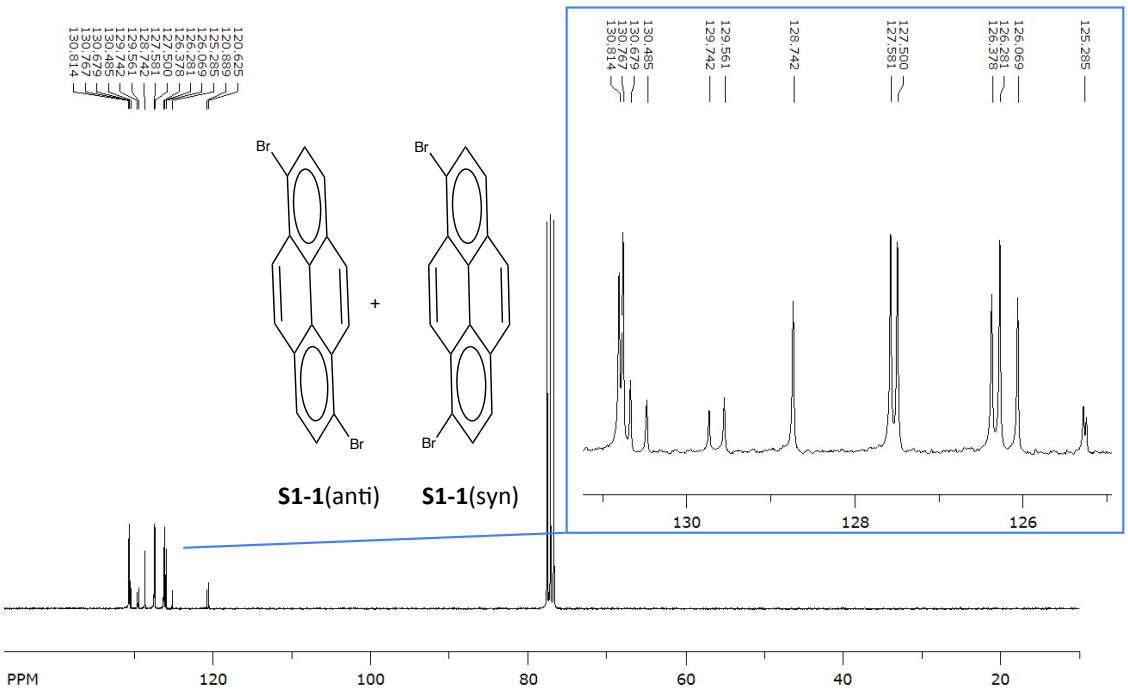

^{1}H NMR spectrum of S1-1(syn) in $CDCl_3$

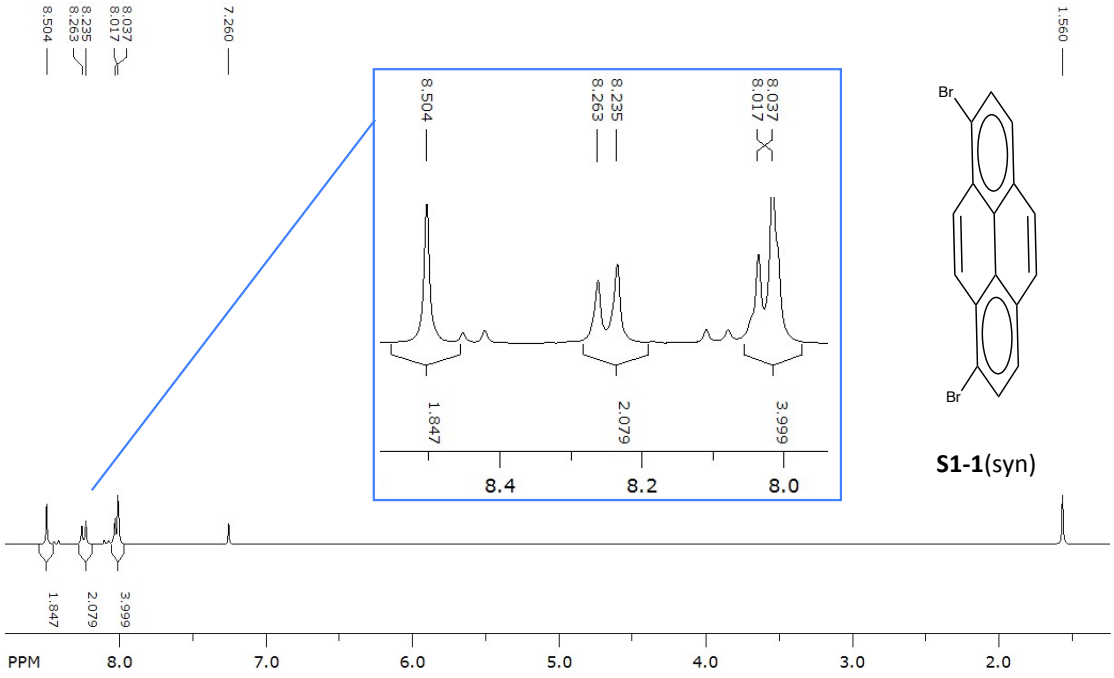

^{1}H NMR spectrum of S1-1(anti) in $CDCl_3$

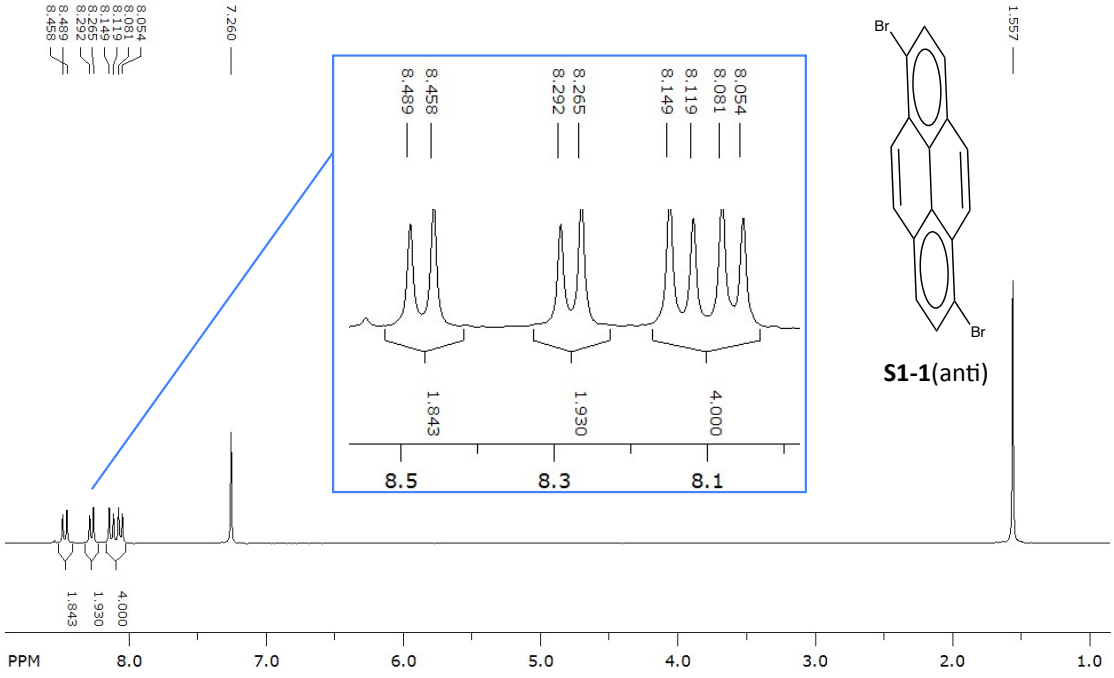

^{1}H NMR spectrum of S1-2 (syn) in $CDCl_3$

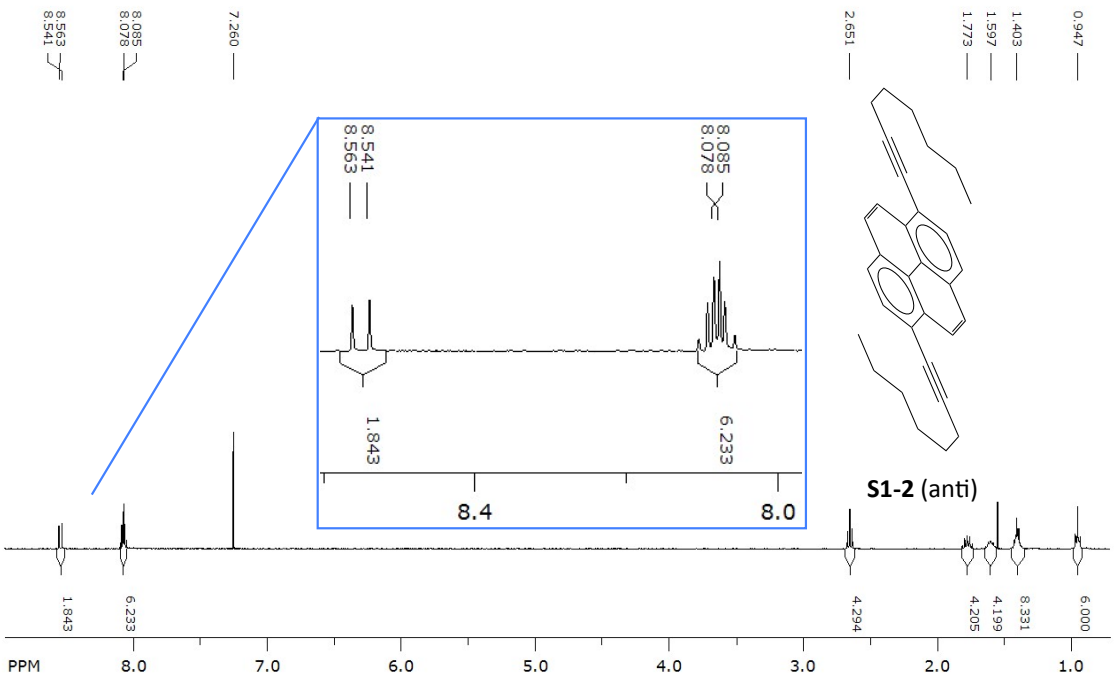

^{1}H NMR spectrum of S1-2 (anti) in $CDCl_3$

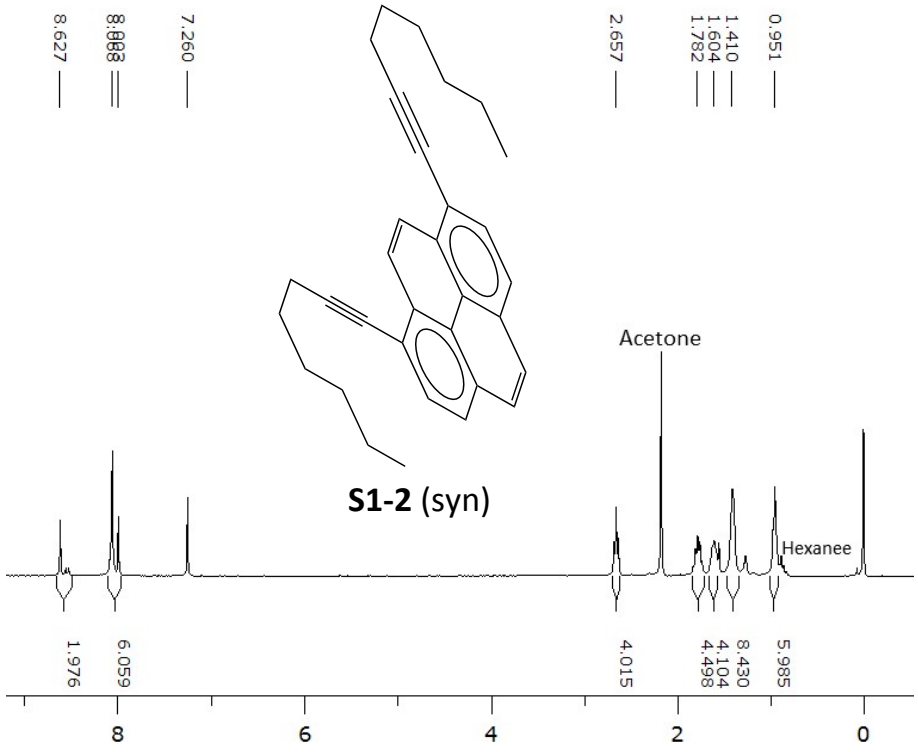

^{1}H NMR spectrum of Py1 in $CDCl_3$

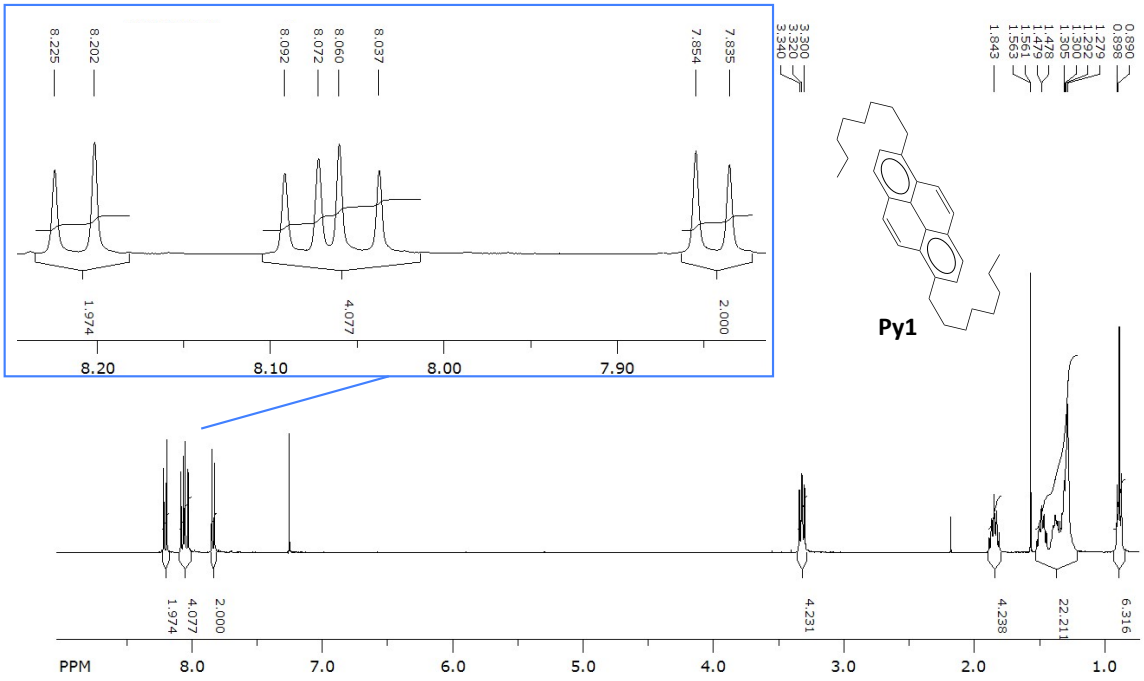

^{13}C NMR spectrum of Py1 in $CDCl_3$

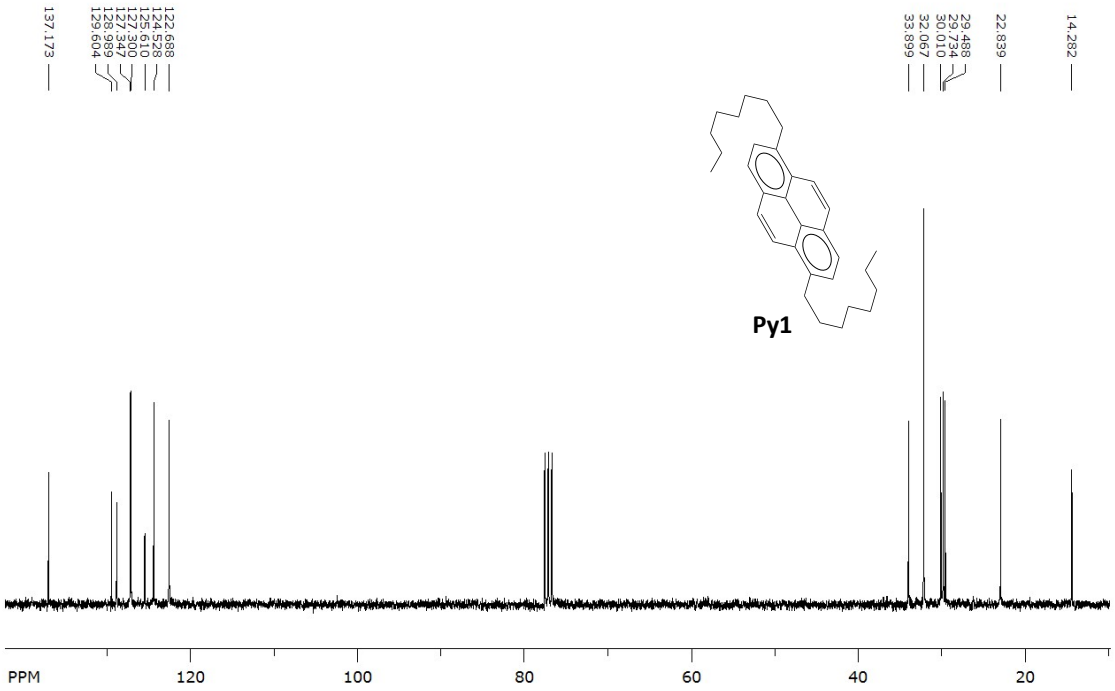

^{1}H NMR spectrum of Py2 in $CDCl_3$

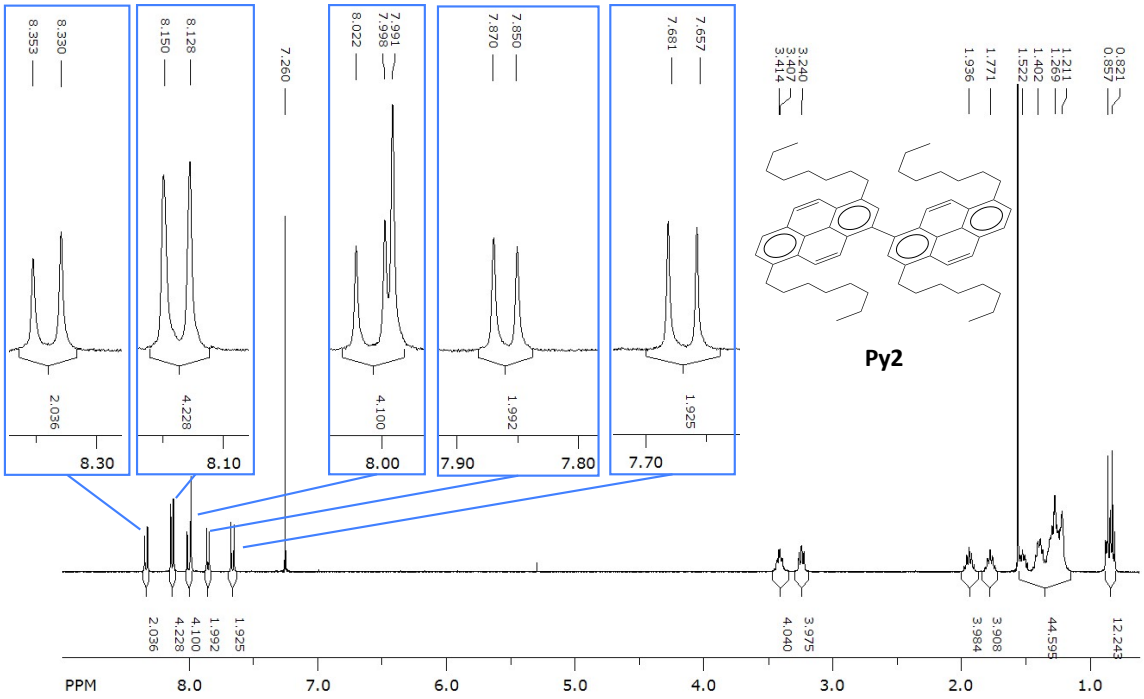

^{13}C NMR spectrum of Py2 in $CDCl_3$

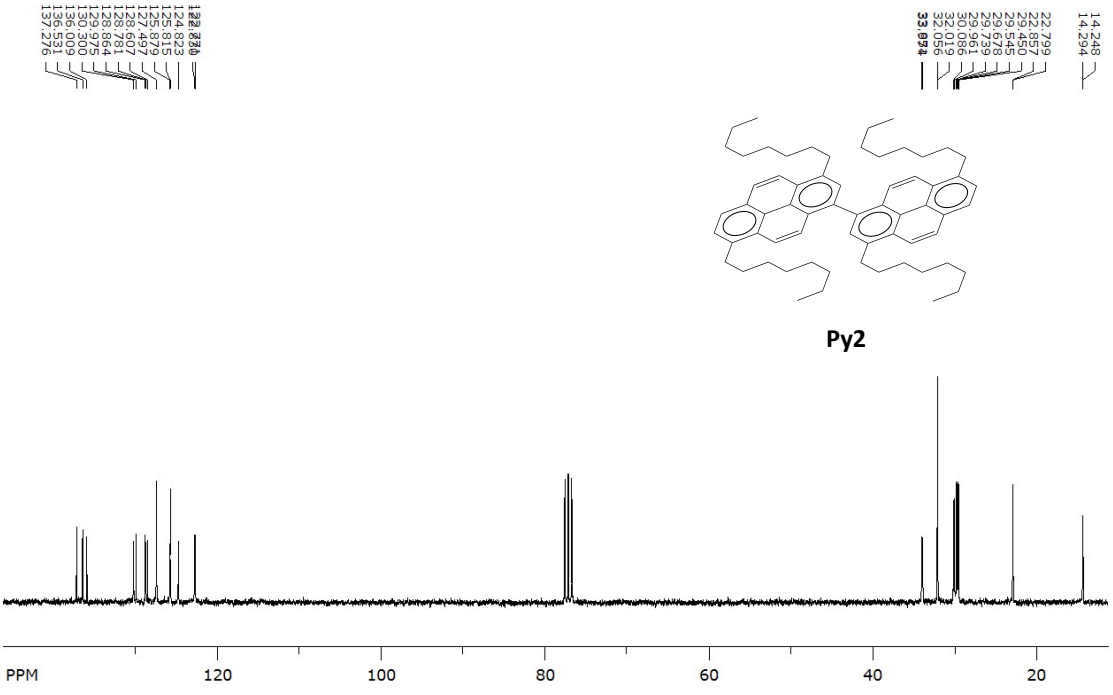

^{1}H NMR spectrum of S3-1 in $CDCl_3$

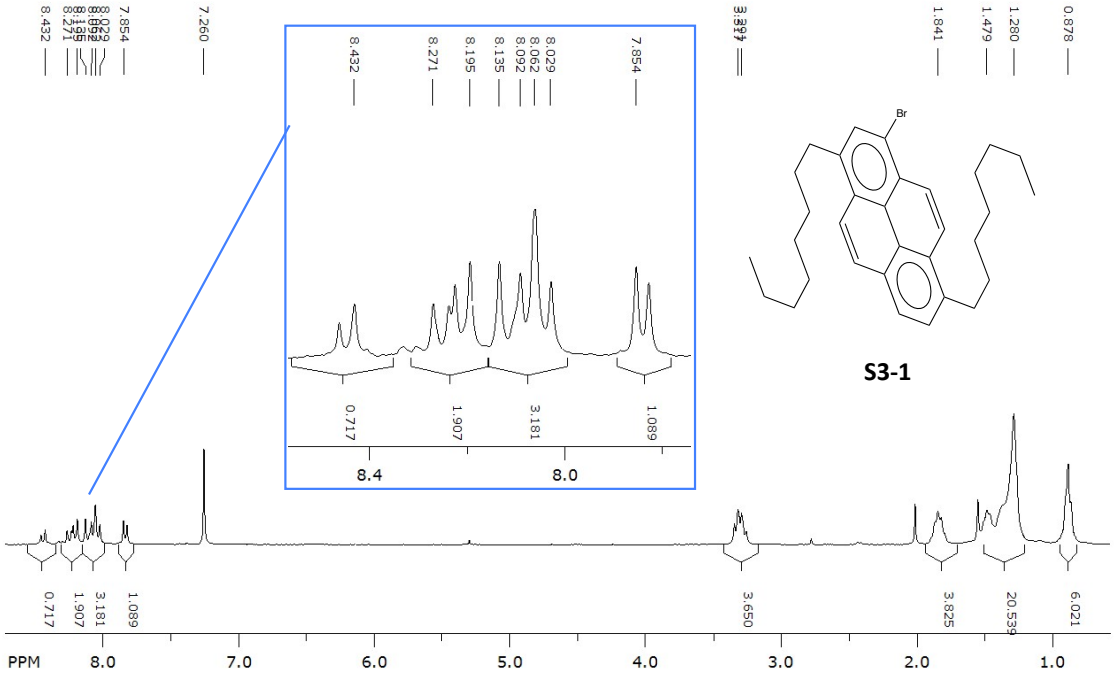

^{13}C NMR spectrum of S3-1 in $CDCl_3$

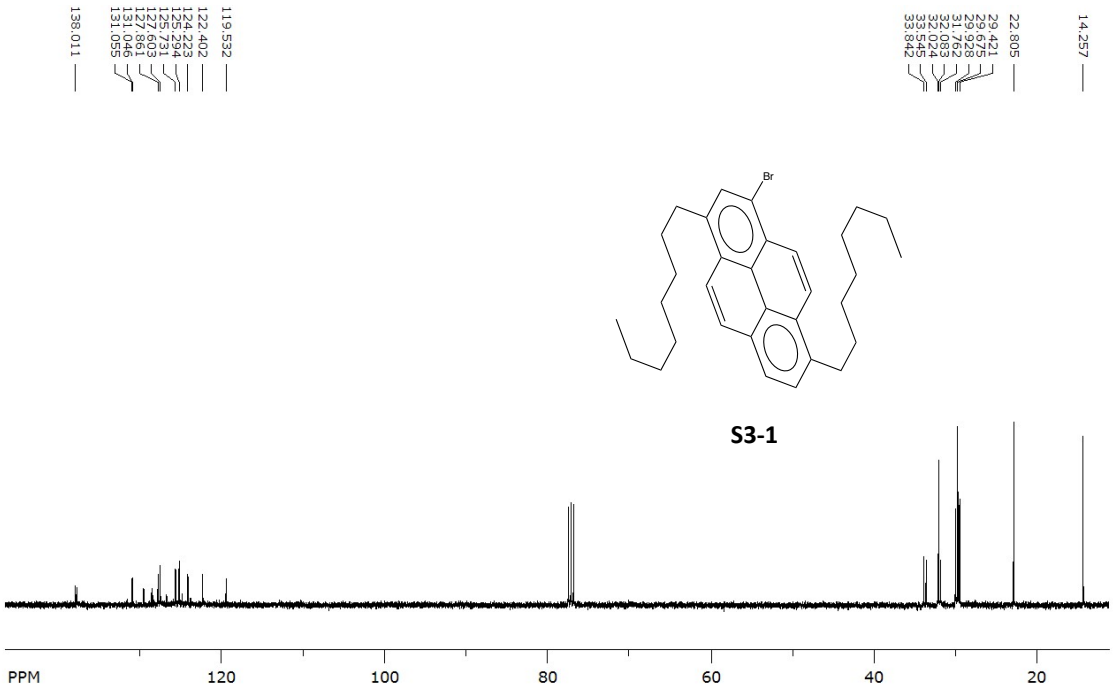

^{1}H NMR spectrum of S3-2 in $CDCl_3$

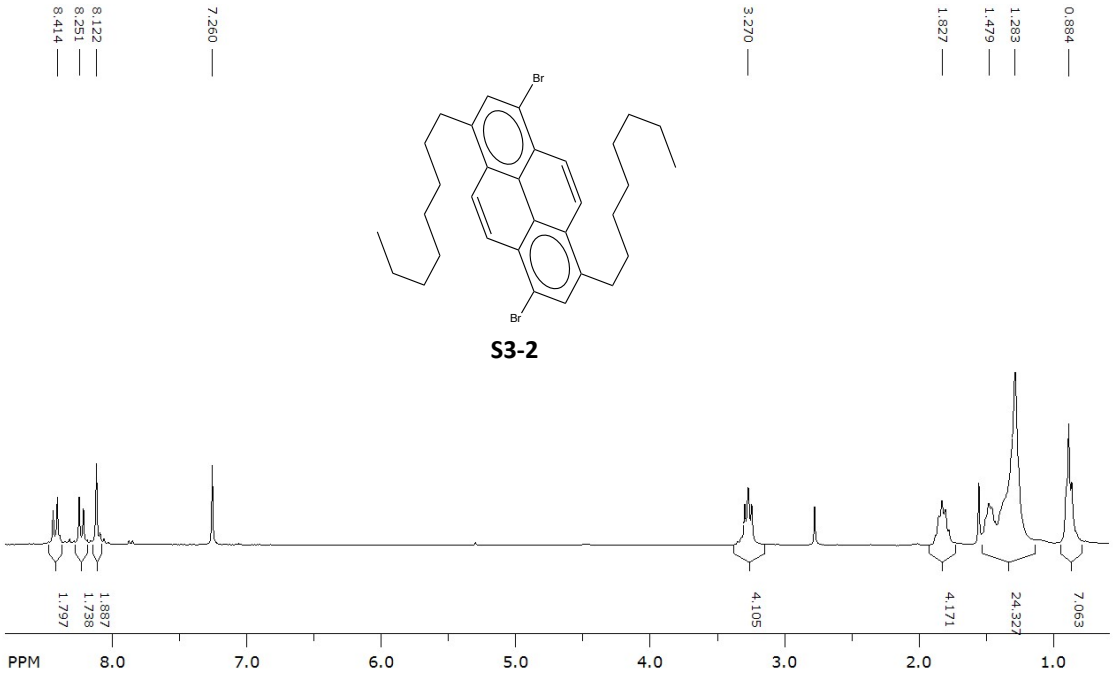

S3-2

^{13}C NMR spectrum of S3-2 in $CDCl_3$

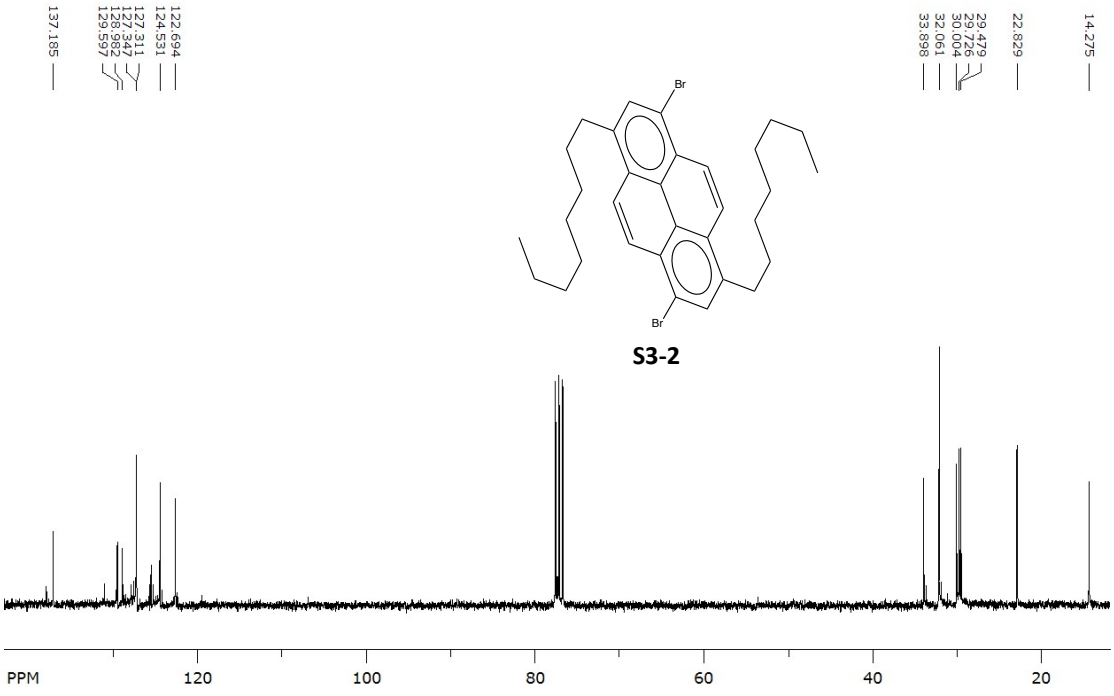

S3-2

^{1}H NMR spectrum of S3-3 in $CDCl_3$

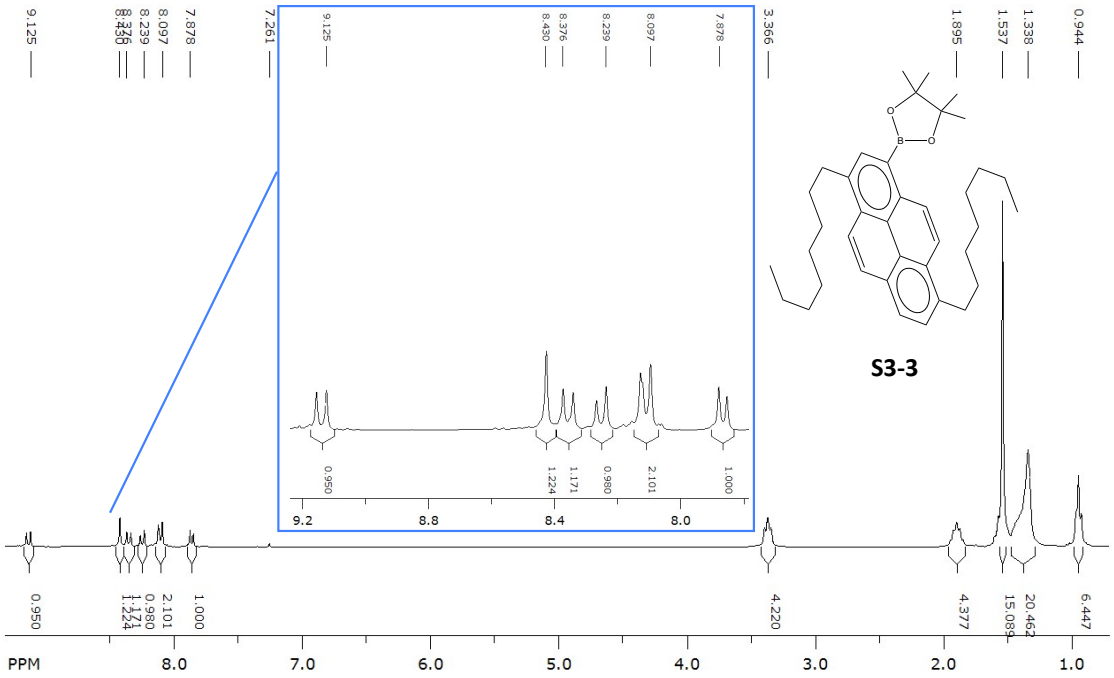

^{13}C NMR spectrum of S3-3 in $CDCl_3$

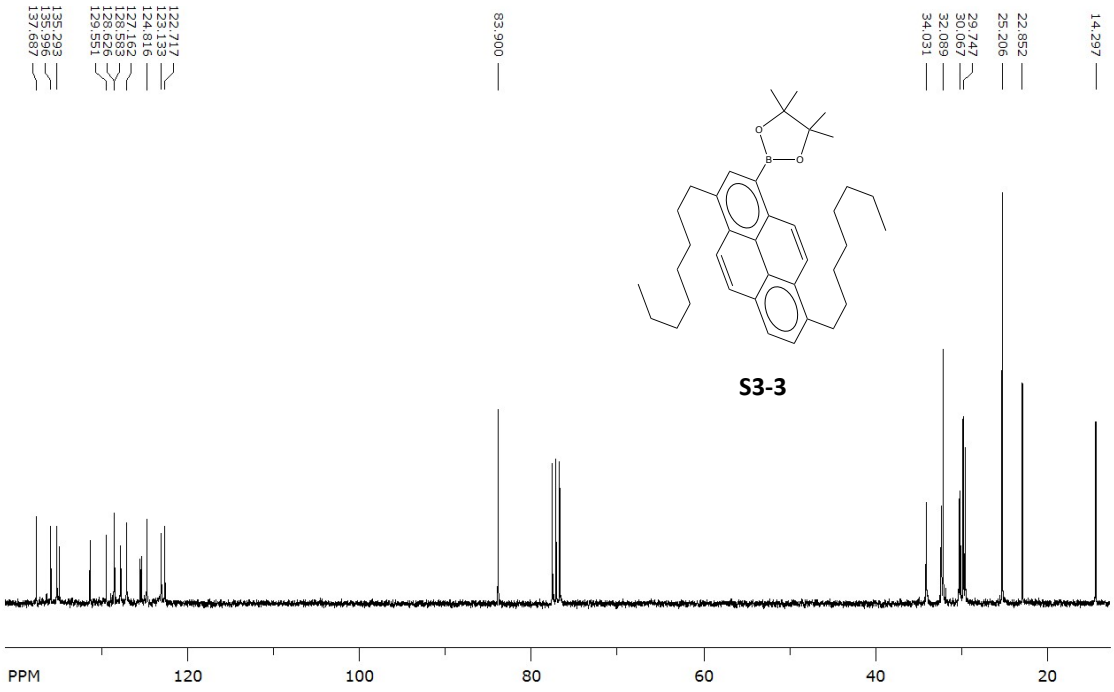

^{1}H NMR spectrum of S3-4 in $CDCl_3$

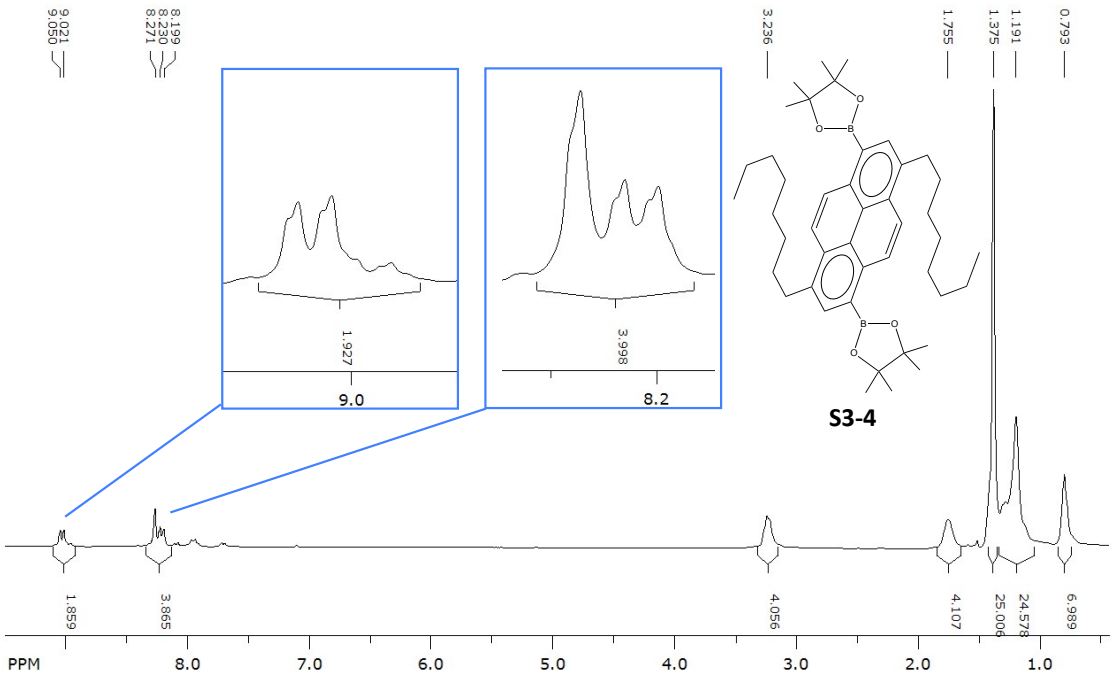

^{13}C NMR spectrum of S3-4 in $CDCl_3$

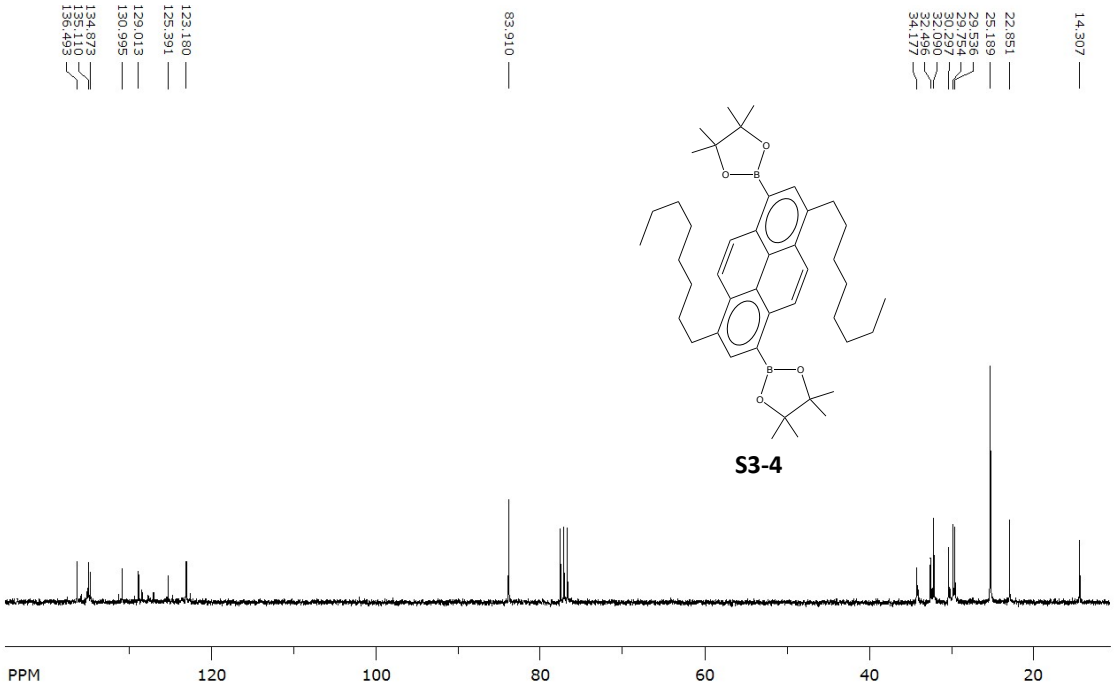

^{1}H NMR spectrum of Py3 in $CDCl_3$

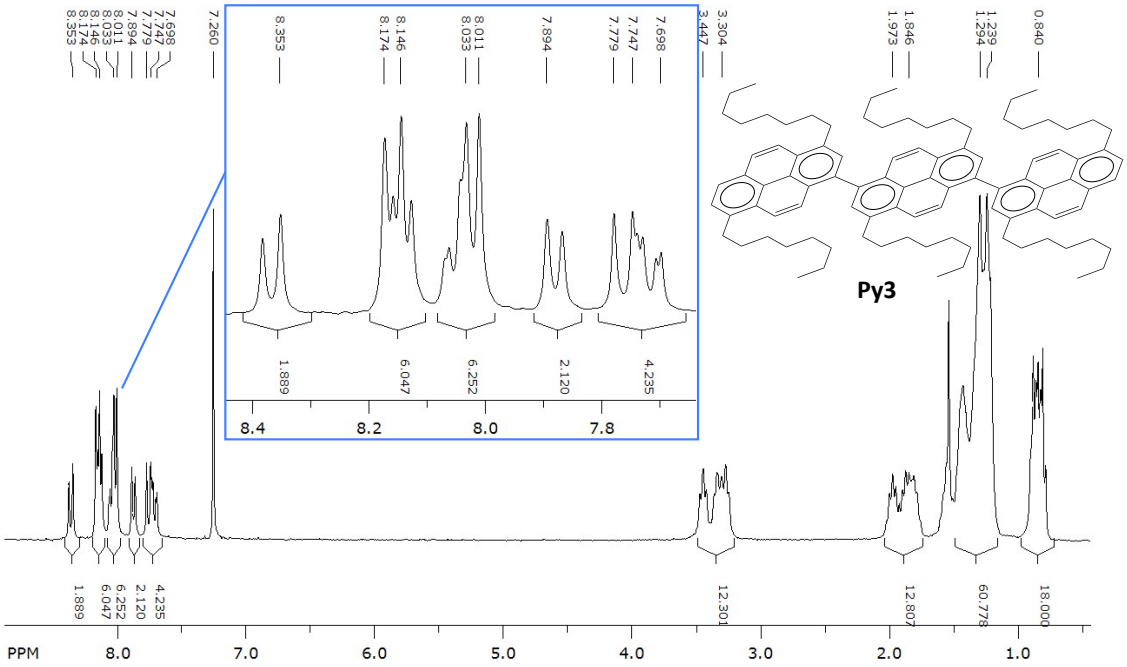

^{13}C NMR spectrum of Py3 in $CDCl_3$

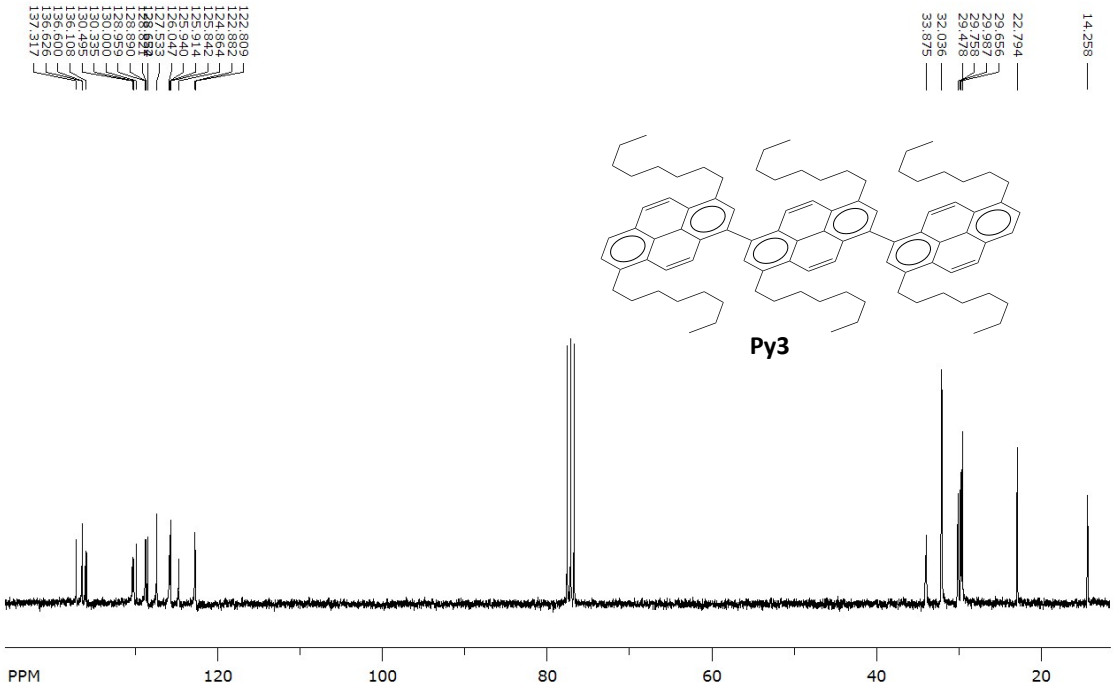

^{1}H NMR spectrum of S4-1 in $CDCl_3$

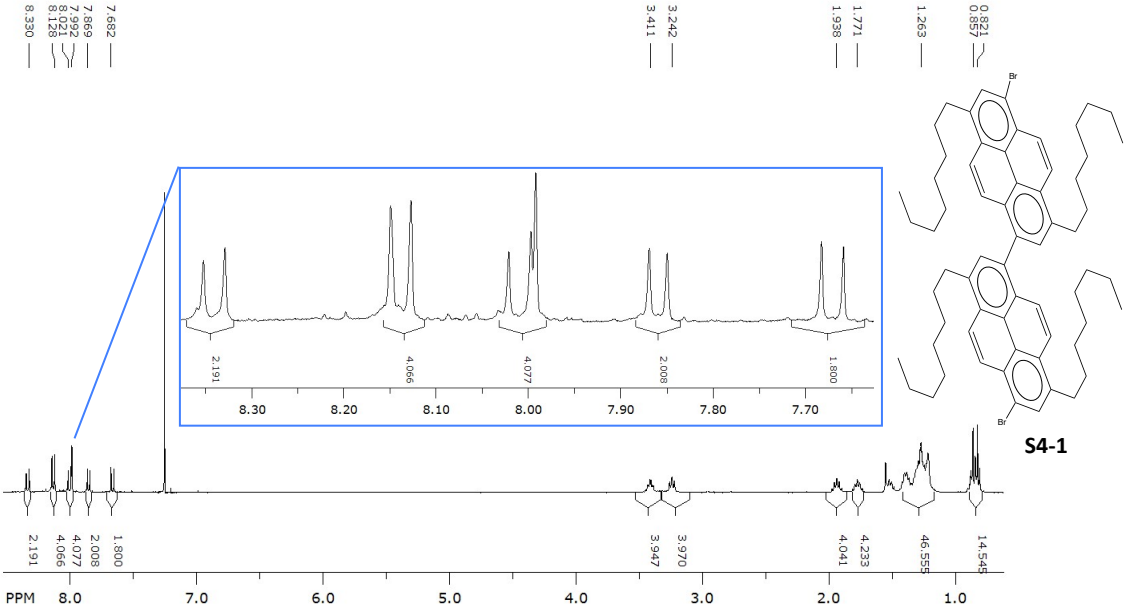

^{13}C NMR spectrum of S4-1 in $CDCl_3$

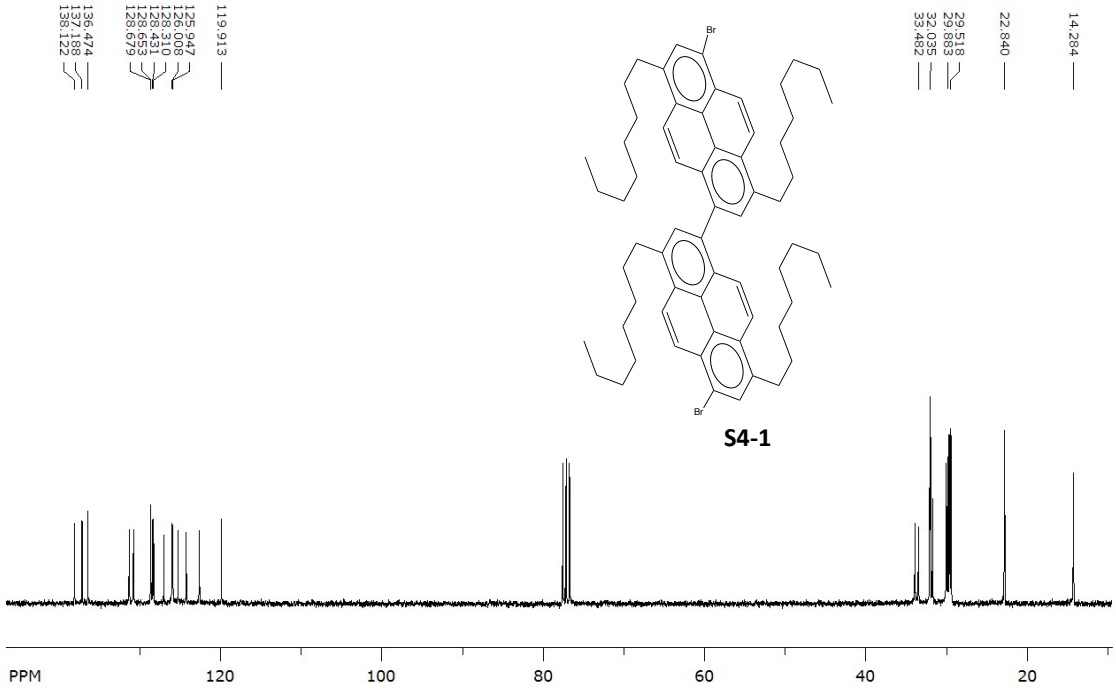

^{1}H NMR spectrum of Py4 in $CDCl_3$

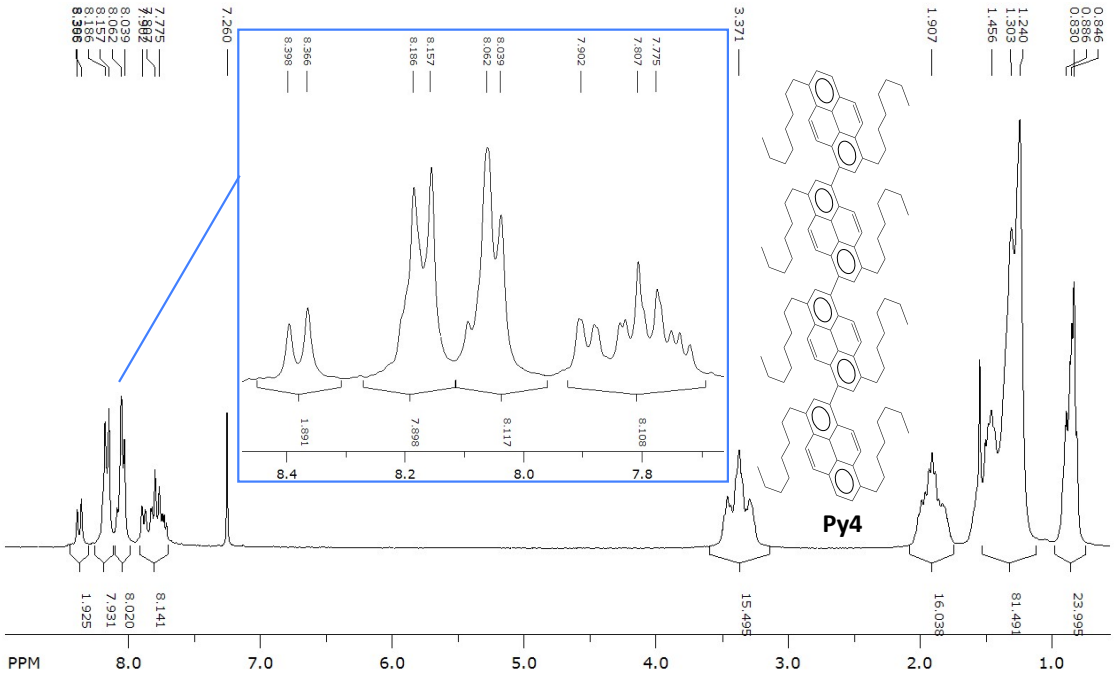

^{13}C NMR spectrum of Py4 in $CDCl_3$

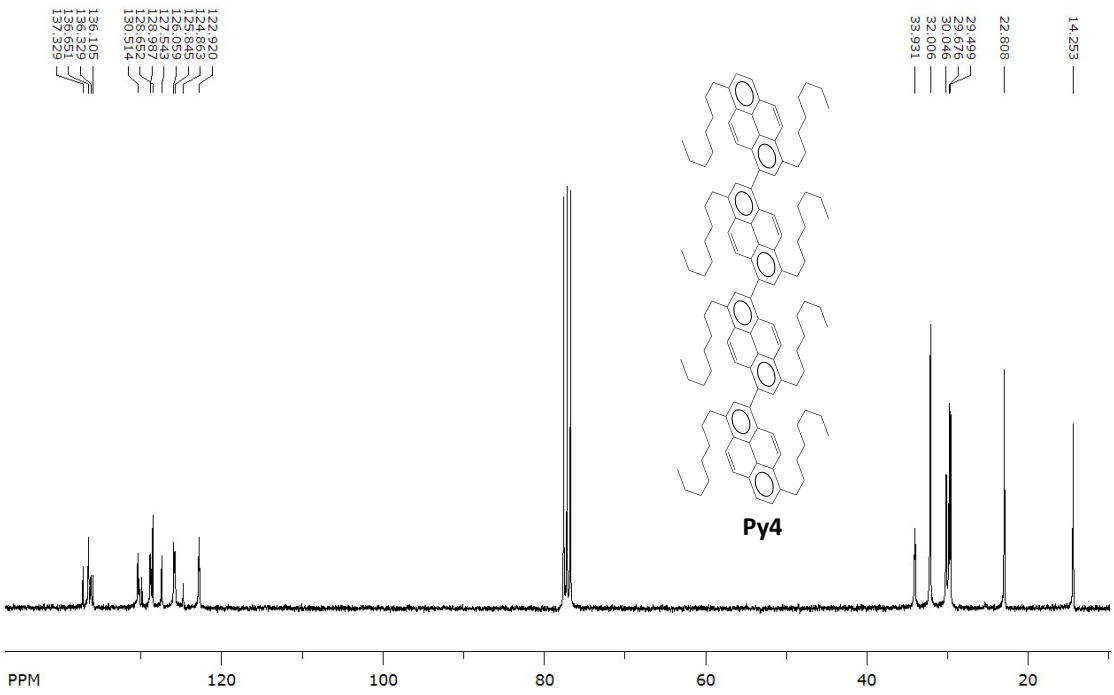

^{1}H NMR spectrum of S5-1 in $CDCl_3$

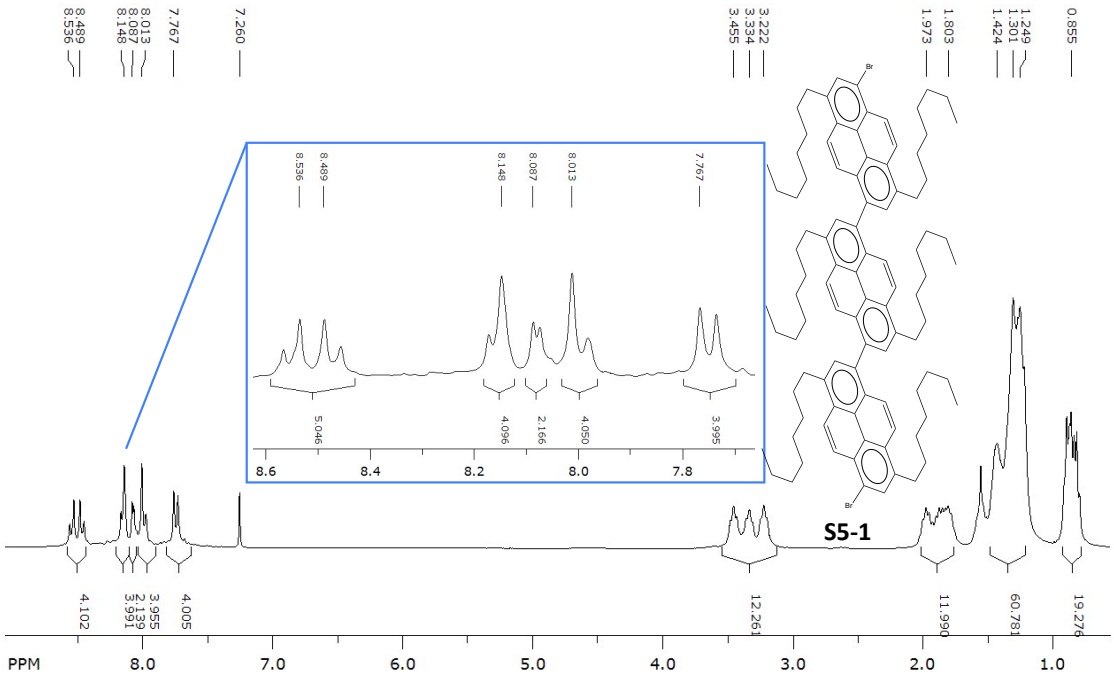

^{13}C NMR spectrum of S5-1 in $CDCl_3$

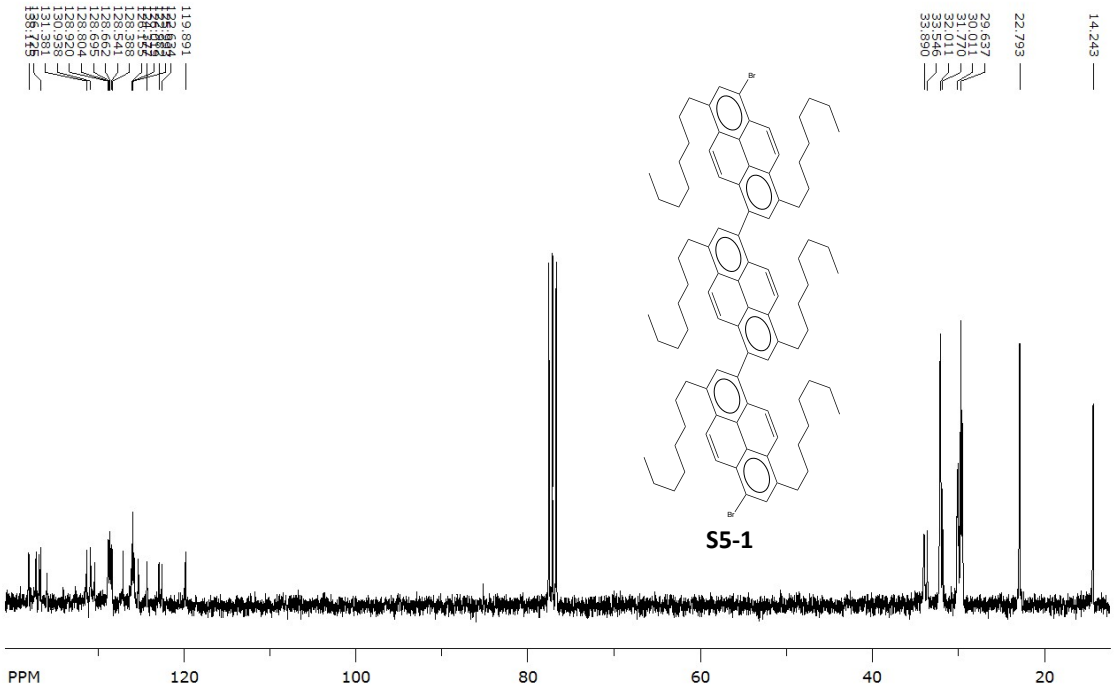

^{1}H NMR spectrum of Py5 in $CDCl_3$

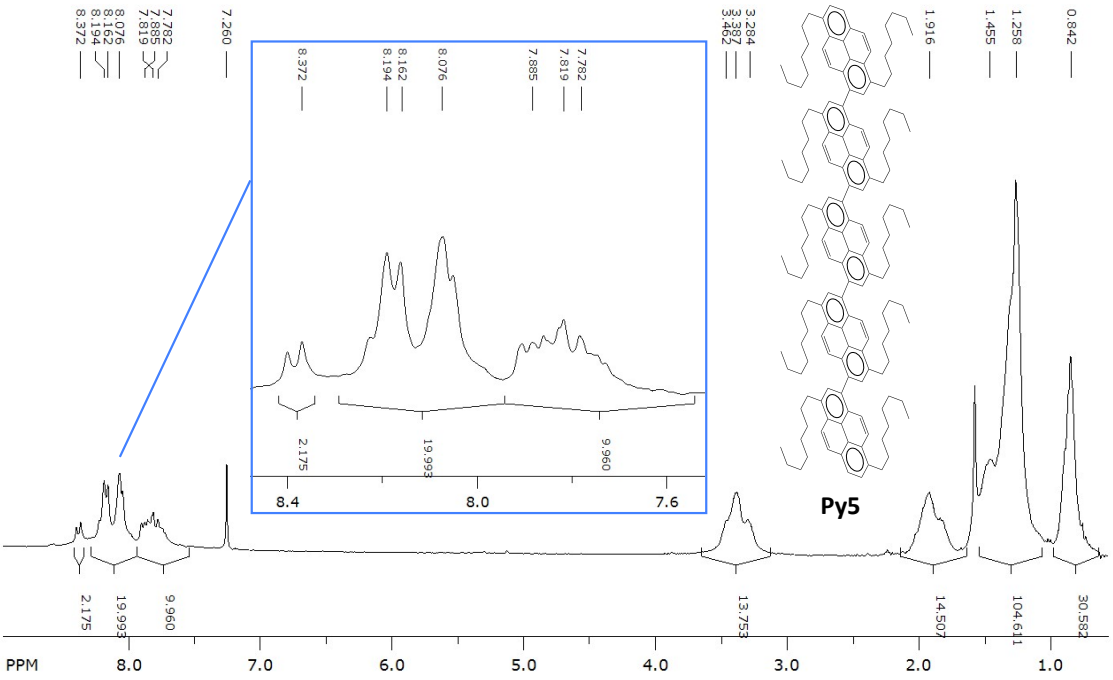

^{13}C NMR spectrum of Py5 in $CDCl_3$

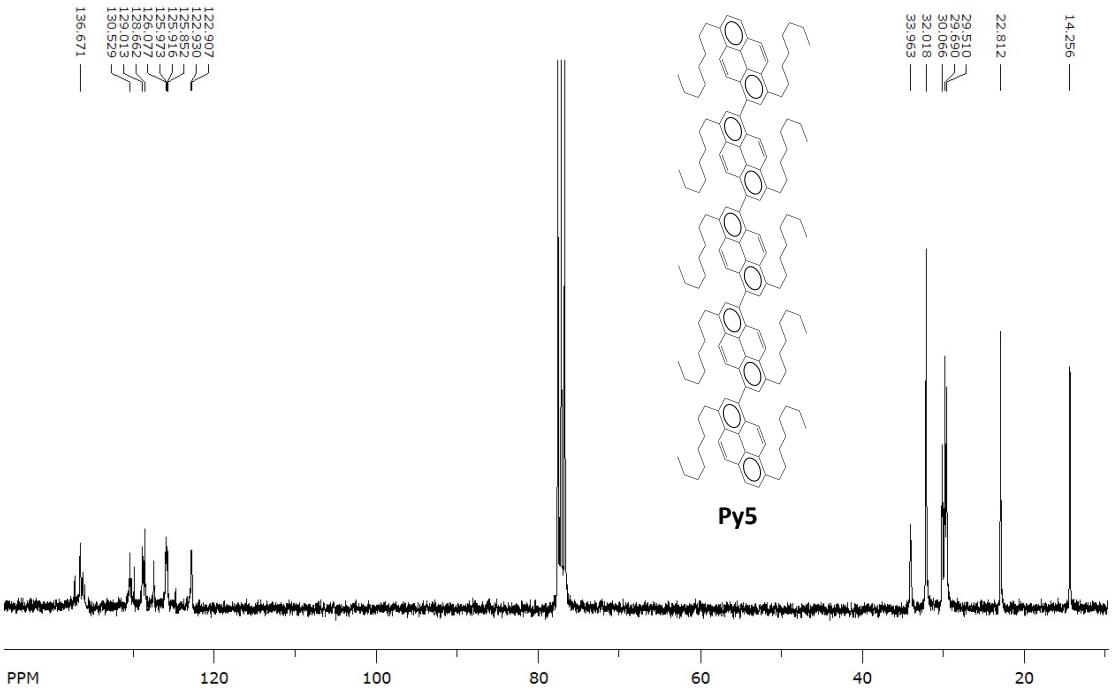

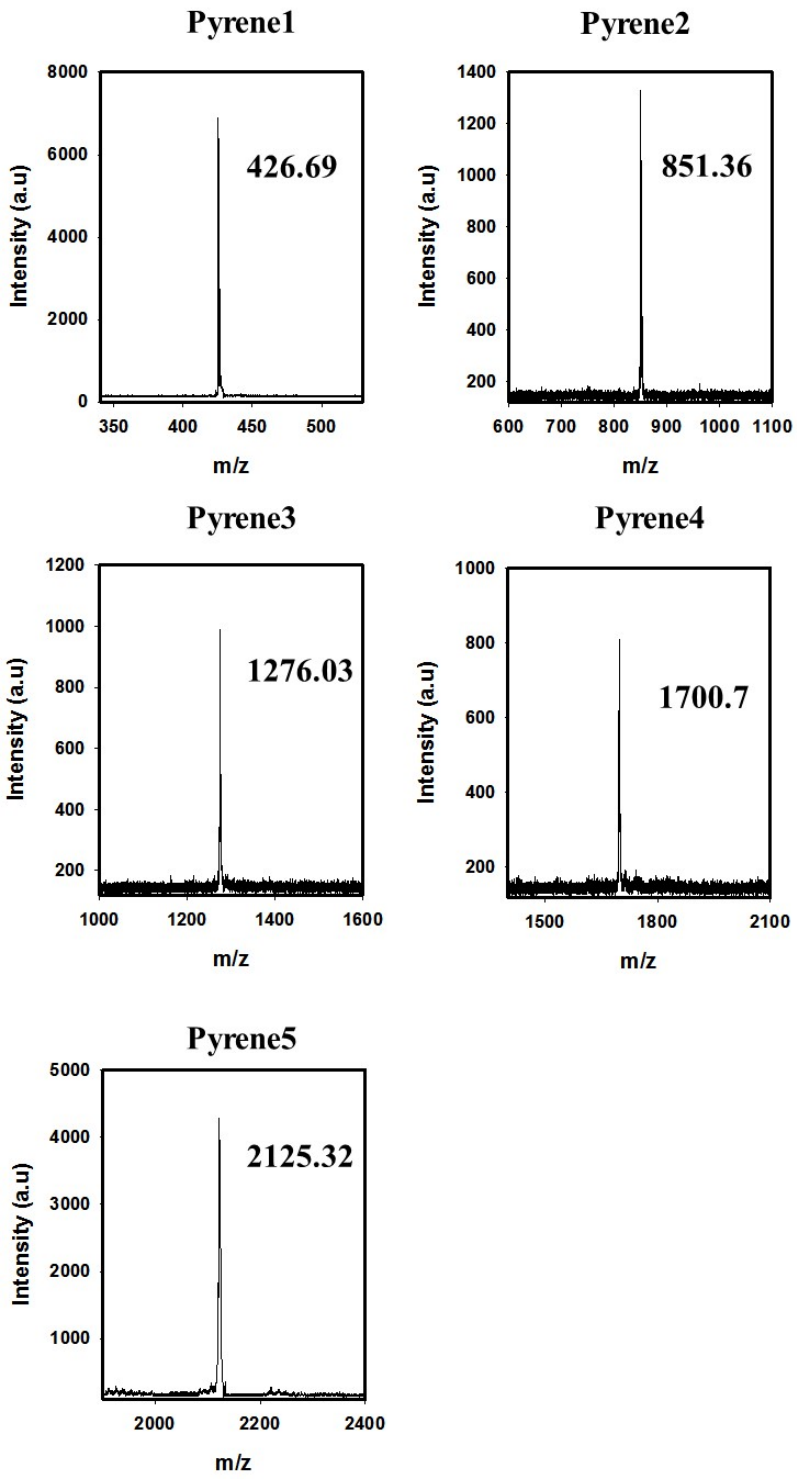

Figure S1. MALDI spectra of *m*-Py$_n$

X-ray crystallography

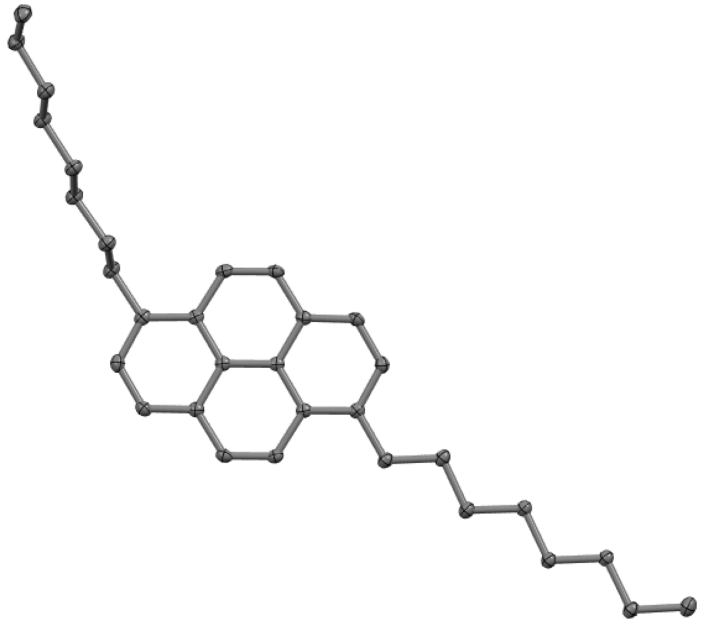

Figure S2. The ORTEP diagrams (50% probability) of **Py**$_1$

Table S1. Crystal data and structure refinement for raj27q.

Identification code	raj27q
Empirical formula	$C_{32}H_{42}$
Formula weight	426.66
Temperature/K	100.00(10)
Crystal system	monoclinic
Space group	$P2_1/n$
a/Å	7.75029(12)
b/Å	34.4156(5)
c/Å	9.25694(17)
α/°	90.00
β/°	94.6142(15)
γ/°	90.00
Volume/Å^3	2461.11(7)
Z	4
ρ_{calc}g/cm^3	1.151
μ/mm^{-1}	0.472
F(000)	936.0
Crystal size/mm^3	0.7503 × 0.1022 × 0.0544

Radiation	CuKα (λ = 1.54184)
2Θ range for data collection/°	9.92 to 148.32
Index ranges	$-9 \le h \le 9$, $-42 \le k \le 42$, $-11 \le l \le 10$
Reflections collected	23509
Independent reflections	4912 [R_{int} = 0.0337, R_{sigma} = 0.0216]
Data/restraints/parameters	4912/0/292
Goodness-of-fit on F^2	1.071
Final R indexes [I>=2σ (I)]	R_1 = 0.0403, wR_2 = 0.1106
Final R indexes [all data]	R_1 = 0.0504, wR_2 = 0.1201
Largest diff. peak/hole / e $Å^{-3}$	0.28/-0.20

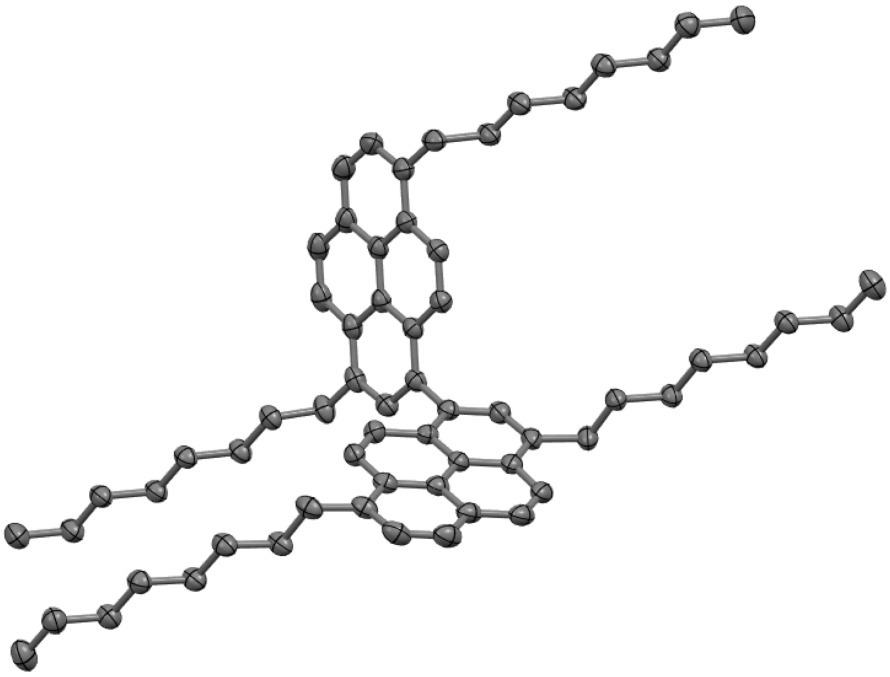

Figure S3. The ORTEP diagrams (50% probability) of *m*-**Py**$_2$.

Table S2. Crystal data and structure refinement for raj27p.

Identification code	raj27p
Empirical formula	$C_{64}H_{82}$
Formula weight	851.30
Temperature/K	99.9(2)
Crystal system	monoclinic
Space group	I2/a
a/Å	16.3409(6)

b/Å	9.0662(3)
c/Å	35.1804(13)
α/°	90.00
β/°	101.985(4)
γ/°	90.00
Volume/Å^3	5098.3(3)
Z	4
ρ_{calc}g/cm^3	1.109
μ/mm^{-1}	0.456
F(000)	1864.0
Crystal size/mm^3	0.1 × 0.05 × 0.03
Radiation	CuKα (λ = 1.54184)
2Θ range for data collection/°	10.08 to 148.38
Index ranges	-20 ≤ h ≤ 20, -11 ≤ k ≤ 11, -38 ≤ l ≤ 43
Reflections collected	23202
Independent reflections	5118 [R_{int} = 0.0379, R_{sigma} = 0.0267]
Data/restraints/parameters	5118/0/291
Goodness-of-fit on F^2	1.023
Final R indexes [I>=2σ (I)]	R_1 = 0.0542, wR_2 = 0.1530
Final R indexes [all data]	R_1 = 0.0832, wR_2 = 0.1822
Largest diff. peak/hole / e Å^{-3}	0.26/-0.19

Synthesis of tert-butylated para-pyrenes

Scheme: Synthesis of 7,7'-di-tert-butyl-2,2'-bipyrene

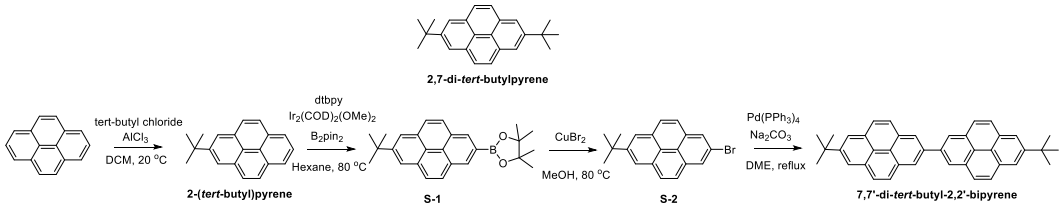

Synthesis of 2-(tert-butyl)pyrene and 2,7-di-tert-butylpyrene:

Both of compounds were prepared according to the published procedure: [1] A mixture of pyrene (5 g, 24.2 mmol) and 2-chloro-2-methylpropane (2.62 g, 3.23 mL, 29 mmol) was added in 40 mL of CH_2Cl_2 at 0 °C and stirred for 15 min. Powdered anhydrous $AlCl_3$ (3.62 g, 27.2 mmol) was slowly added to a stirred solution. The reaction mixture was continuously stirred for 3 h at room temperature, and then poured into a large excess of ice/water. The reaction mixture was extracted with dichloromethane (2 x 50 mL). The combined organic extracts were washed by water and brine, dried with anhydrous $MgSO_4$ and evaporated. The residue was crystallized from Methanol to give pure 2,7-di-*tert*-butylpyrene as white color solid (1.02 g, 3.24 mmol, 11.2 % yield). M.p. 208-210 ºC.^{1}H NMR (400 MHz, $CDCl_3$) δ ppm 1.59 (s, 18H), 8.03 (s, 4H), 8.19 (s, 4H); ^{13}C NMR (75 MHz, $CDCl_3$) δ ppm 32.12, 35.35, 122.13, 122.98, 127.55, 130.89, 148.68.

The mother liquor was concentrated under reduced pressure and dissolved in a minimal amount of boiling hexanes (20 mL). The mixture was left to recrystallize overnight in the freezer. Filtration offered the 2-*tert*-butylpyrene as a white solid (3.37 g, 13.1 mmol, 45.2 % yield). M.p. 111-113°C. ^{1}H NMR (400 MHz, $CDCl_3$) δ ppm 1.60 (s, 9H), 7.97 (t, *J* = 8.0 Hz, 1H), 8.06 (s, 4H), 8.16 (d, *J* = 8.0 Hz, 2H), 8.23 (s, 2H); ^{13}C NMR (75 MHz, $CDCl_3$) δ ppm 32.10, 35.38, 122.13, 122.35, 123.02, 124.74, 124.86, 125.63, 127.38, 127.70, 131.09, 149.13

Synthesis of 2-(7-(tert-butyl)pyren-2-yl)-4,4,5,5-tetramethyl-1,3,2-dioxaborolane (S-1):

Compound S-1 was prepared according to the published procedure: [1] 2-*tert*-butyl-pyrene (3.0 g, 11.6 mmol, 1 equiv.), B_2pin_2 (1.55 g, 5.8 mmol, 0.5 equiv.), 4,4-di-*tert*-butyl-2,2-bipyridine (dtbpy) (62 mg, 0.23 mmol, 2 mol %) and dry hexane (30 mL) were added to a dry round bottom flask under Argon atmosphere. The catalyst $Ir_2(COD)_2(OMe)_2$] (78 mg, 0.11 mmol, 1 mol %) was then added and the reaction set to 80 ºC for 6 h. The reaction mixture was concentrated under reduced pressure and purified by flash column chromatography (100 % hexanes to 75 % dichloromethane/hexanes) to afford pure S-1 product as a white color solid (3.2 g, 8.35 mmol, 72 % yield). M.p. 218-219 ºC. ^{1}H NMR (400 MHz, $CDCl_3$) δ ppm 1.46 (s, 12H), 1.58 (s, 9H), 8.03 (d, *J* = 9.0 Hz, 2H), 8.07 (d, *J* = 9.0 Hz, 2H), 8.20 (s, 2H), 8.60 (s, 2H); ^{13}C NMR (75 MHz, $CDCl_3$) δ ppm 25.15, 32.07, 35.42, 84.24, 122.24, 122.96, 126.46, 127.57, 127.77, 130.37, 131.28, 131.60, 149.70.

Synthesis of 2-Bromo-7-(tert-butyl)pyrene (S-2):

Compound S-2 was prepared according to the published procedure: [1] 2-(7-(*tert*-butyl)pyrene-2-yl)-4,4,5,5-tetramethyl-1,3,2-dioxaborolane (S-1) (1.62 g, 4.21 mmol, 1 equiv.) and dry methanol (48 mL) were added to a dry round bottom flask. The reaction mixture was heated to 80 °C to fully dissolve S-1 and then $CuBr_2$ (2.83 g, 12.6 mmol, 3 equiv.) was added. The reaction was left to stir for 24 h at 80 °C. Then, the reaction mixture was concentrated under reduced pressure and purified by flash column chromatography (100 % hexanes) to afford the desired product as white solid S-2 (1.04 g, 3.08 mmol, 73.2 %). M.p. 141-143 ºC. ^{1}H NMR (400 MHz, $CDCl_3$) δ ppm 1.59 (s, 9H), 7.94 (d, *J* = 9.0 Hz, 2H), 8.07 (d, *J* = 9.0 Hz, 2H), 8.24 (s, 4H); ^{13}C NMR (75 MHz, $CDCl_3$) δ ppm 32.05, 35.44, 119.65, 122.14, 122.64, 123.13, 126.26, 126.98, 128.94, 130.78, 132.64, 149.59.

Synthesis of 7,7'-di-tert-butyl-2,2'-bipyrene:

2-(7-(*tert*-butyl)pyren-2-yl)-4,4,5,5-tetramethyl-1,3,2-dioxaborolane (S-1) (384 mg, 1.0 mmol), 2-Bromo-7-(*tert*-butyl)pyrene (S-2) (337 mg, 1.0 mmol) and 20 mL of 1,2-dimethoxyethane were placed in a 100 mL Schlenk flask under an argon atmosphere. The degassed Na_2CO_3 (1.06g in 10 mL of H_2O) solution was added to the mixture, then catalyst $Pd(PPh_3)_4$ (35 mg) was also added to the flask. The mixture was degassed three times and refluxed for 12 hour. After the reaction was finished, the mixture was poured into 100 mL of water, then extracted with dichloromethane (2×50 mL). The organic layer was dried over $MgSO_4$ and evaporated. The crude product was purified by flash column chromatography (100% hexanes to 5% EtOAc/hexanes) to afford the desired product as a pure white solid (289 mg, 0.56 mmol, 56%). M.p. 370-372 ºC. 1H NMR (400 MHz, $CDCl_3$): 1.62 (s, 18H), 8.12 (d, *J* = 9.0 Hz, 4H), 8.19 (d, *J* = 9.0 Hz, 4H), 8.26 (s, 4H), 8.66 (s, 4H). 13C NMR (75 MHz, $CDCl_3$): 32.13, 35.45, 122.61, 123.00, 124.02, 124.54, 127.63, 128.22, 131.16, 131.70, 139.11, 149.30.

Scheme: Synthesis of 7,7'-di-tert-butyl-1,1'-bipyrene:[2]

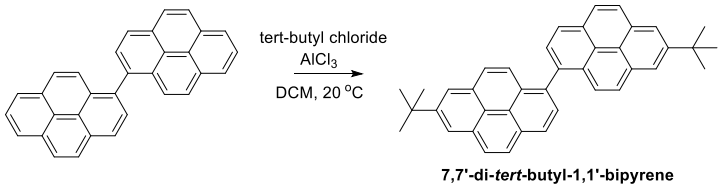

A mixture of 1,1'-bipyrene (0.8 g, 2 mmol, 1.0 eq) and 2-chloro-2-methylpropane (0.425 g, 0.5 mL, 4.4 mmol, 2.2 eq) was added in 20 mL of CH_2Cl_2 at 0 °C and stirred for 15 min. Powdered anhydrous $AlCl_3$ (0.56 g, 4.2 mmol, 2.1 eq) was slowly added to a stirred solution. The reaction mixture was continuously stirred for 3 h at room temperature, and then poured into a large excess of ice/water. The reaction mixture was extracted with dichloromethane (2 x 20 mL). The combined organic extracts were washed by water and brine, dried with anhydrous $MgSO_4$ and evaporated. The crude product was purified by flash column chromatography (100% hexanes to 5% EtOAc/hexanes) to afford the desired product as a yellow color solid (672 mg 1.31 mmol, 65%). M.p. 216-218 ºC. ^{1}H

NMR ($CDCl_3$): 1.59 (s, 18H), 7.61 (d, *J* = 9.2 Hz, 2H), 7.85 (d, *J* = 9.2 Hz, 2H), 8.11-8.18 (m, 8H), 8.28 (d, *J* = 1.7 Hz, 2H), 8.33 (d, *J* = 7.8 Hz, 2H). ^{13}C NMR ($CDCl_3$): 32.08, 35.39, 122.45, 122.63, 123.17, 124.48, 124.84, 125.88, 127.49, 127.84, 127.89,128.60, 129.98, 130.84, 130.96, 131.48, 136.33, 149.38.

^1H NMR spectrum of 2-(*tert*-butyl)pyrene in $CDCl_3$

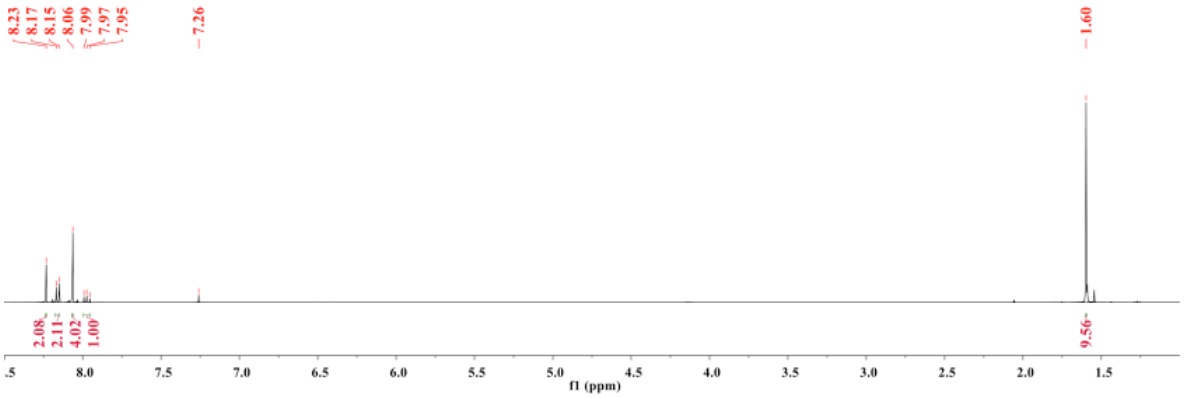

^{13}C NMR spectrum of 2-(*tert*-butyl)pyrene in $CDCl_3$

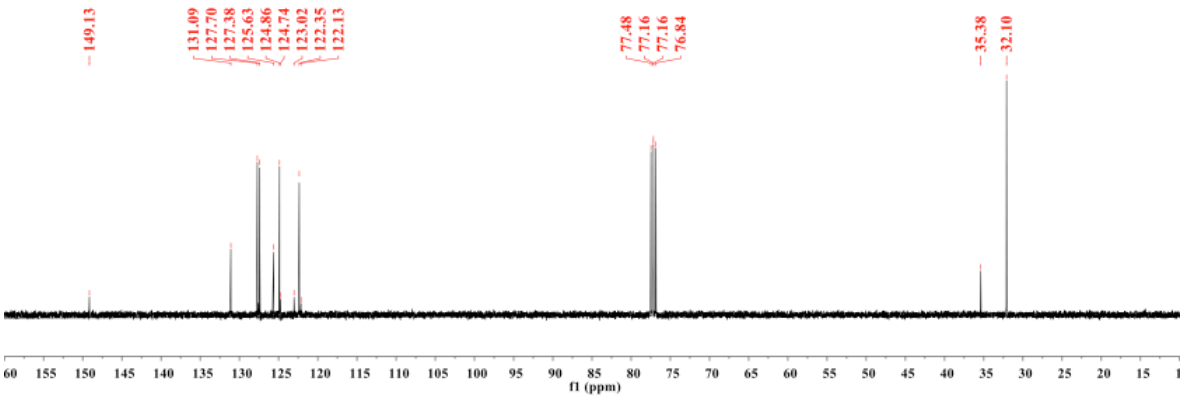

^1H NMR spectrum of 2,7-di-*tert*-butylpyrene in $CDCl_3$

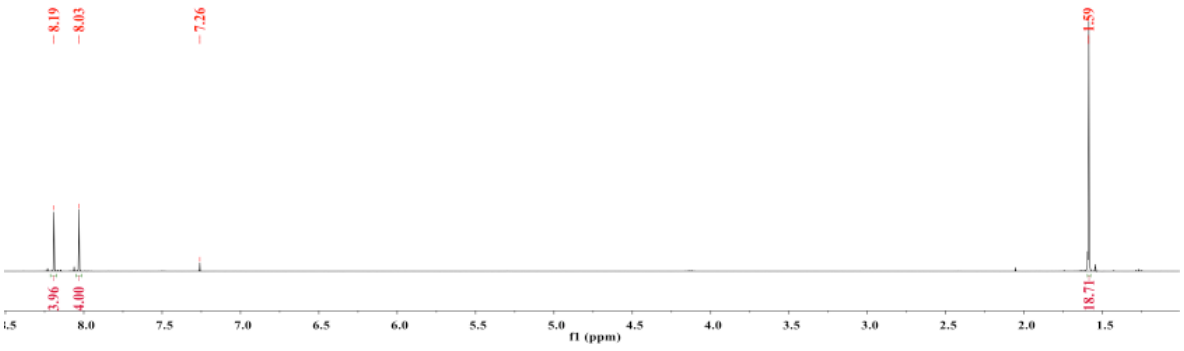

^{13}C NMR spectrum of 2,7-di-*tert*-butylpyrene in $CDCl_3$

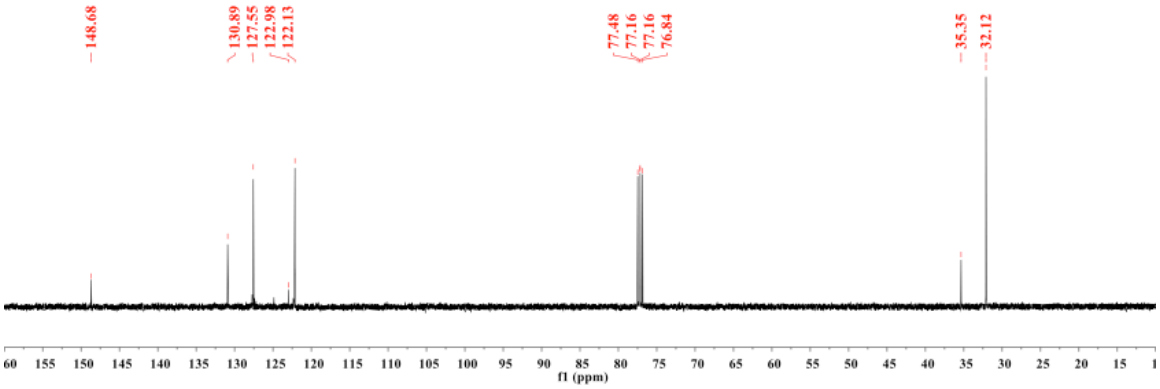

^{1}H NMR spectrum of S-1 in $CDCl_3$

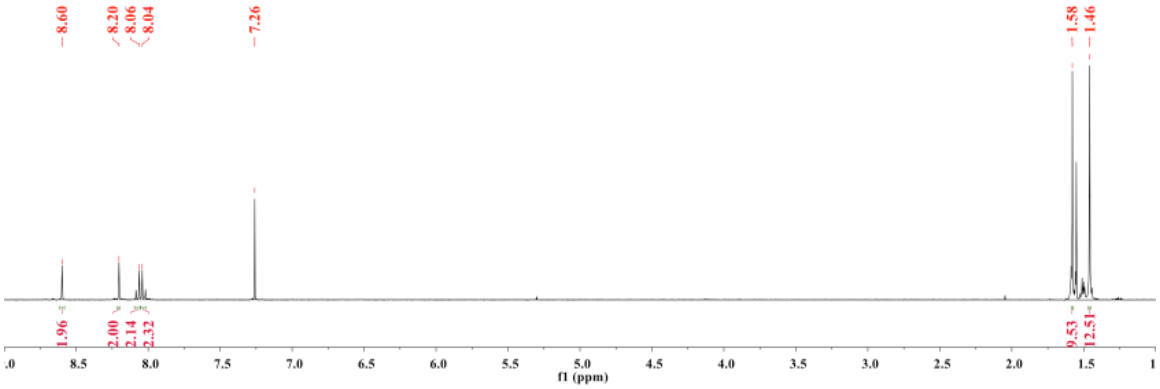

^{13}C NMR spectrum of S-1 in $CDCl_3$

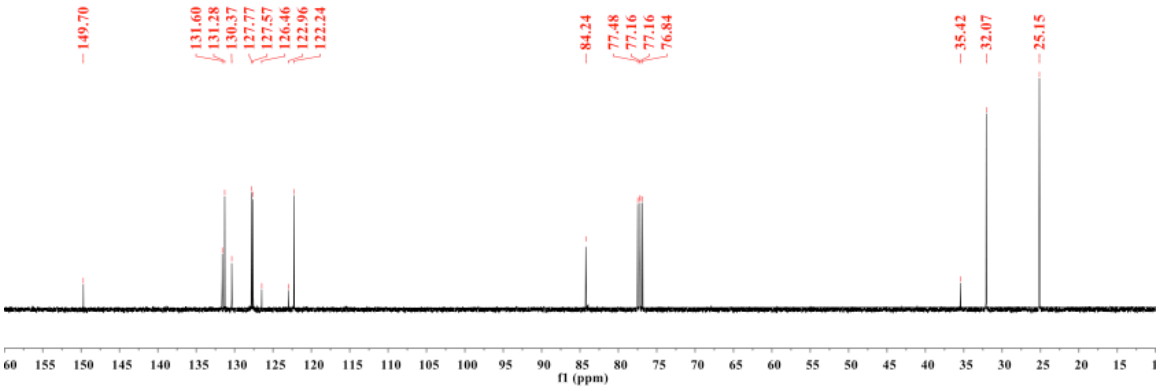

^{1}H NMR spectrum of S-2 in $CDCl_3$

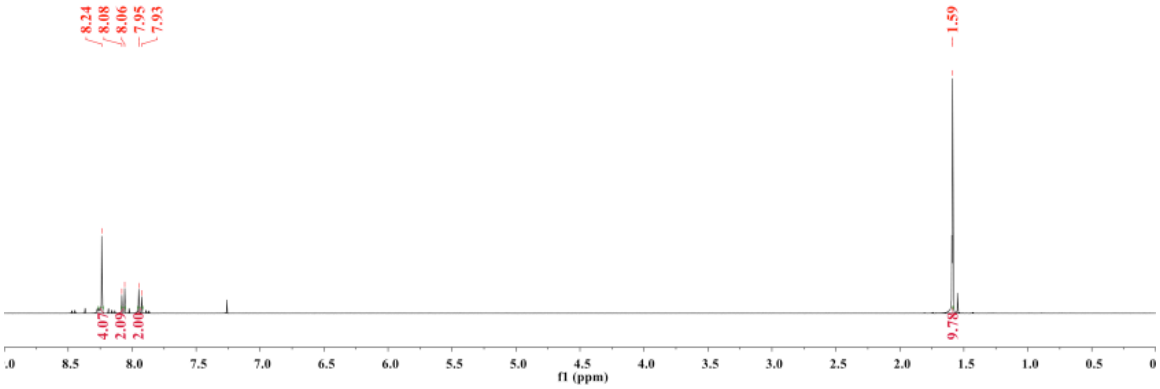

^{13}C NMR spectrum of S-2 in $CDCl_3$

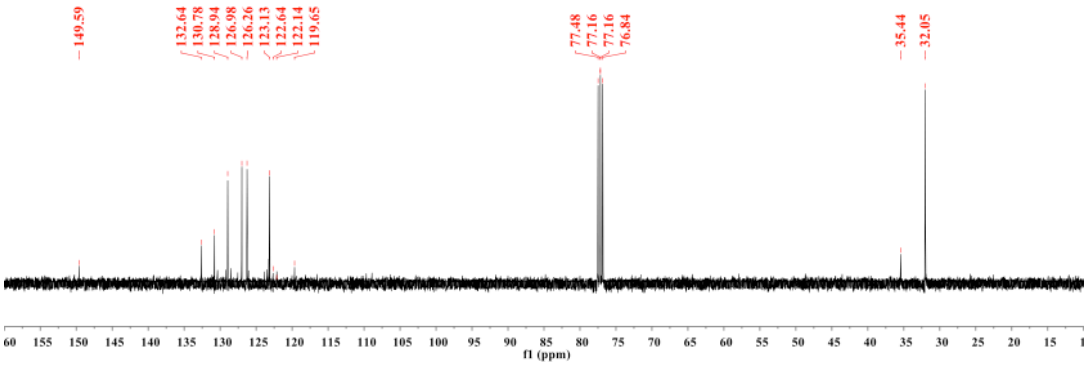

^{1}H NMR spectrum of 7,7'-di-*tert*-butyl-2,2'-bipyrene in $CDCl_3$

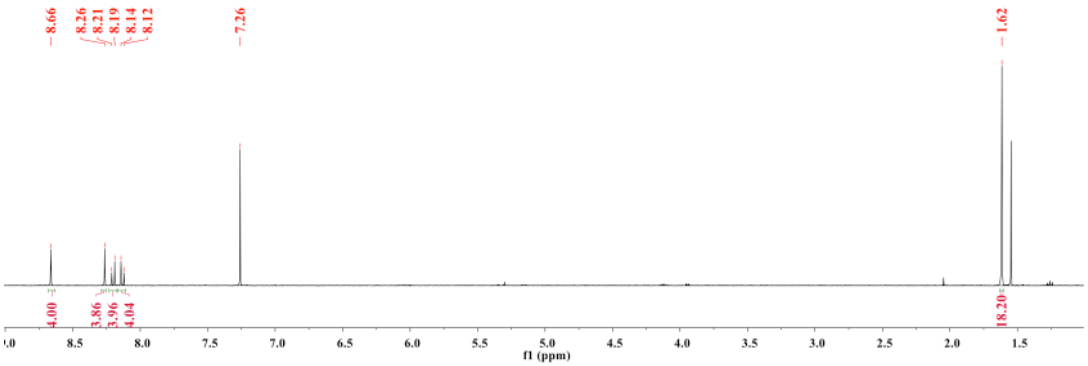

^{13}C NMR spectrum of 7,7'-di-*tert*-butyl-2,2'-bipyrene in $CDCl_3$

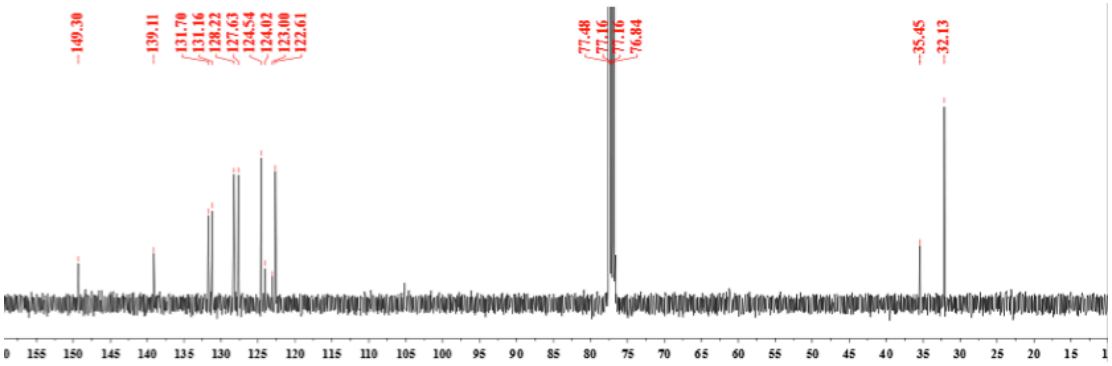

^{1}H NMR spectrum of 7,7'-di-*tert*-butyl-1,1'-bipyrene in $CDCl_3$

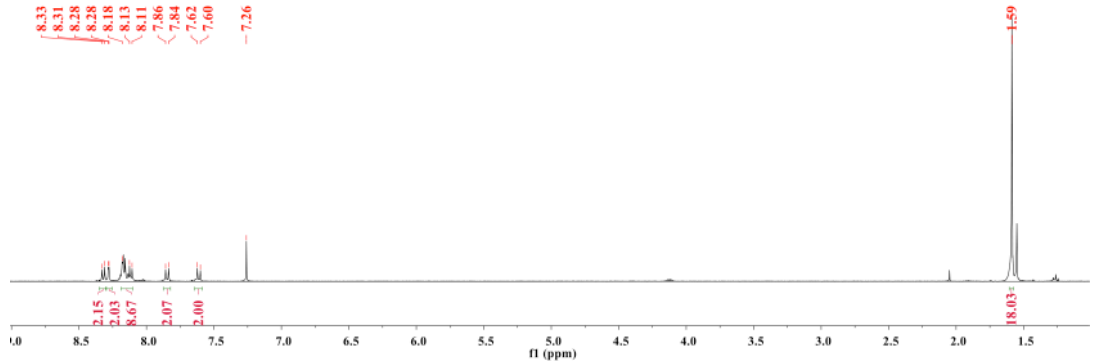

^{13}C NMR spectrum of 7,7'-di-*tert*-butyl-1,1'-bipyrene in $CDCl_3$

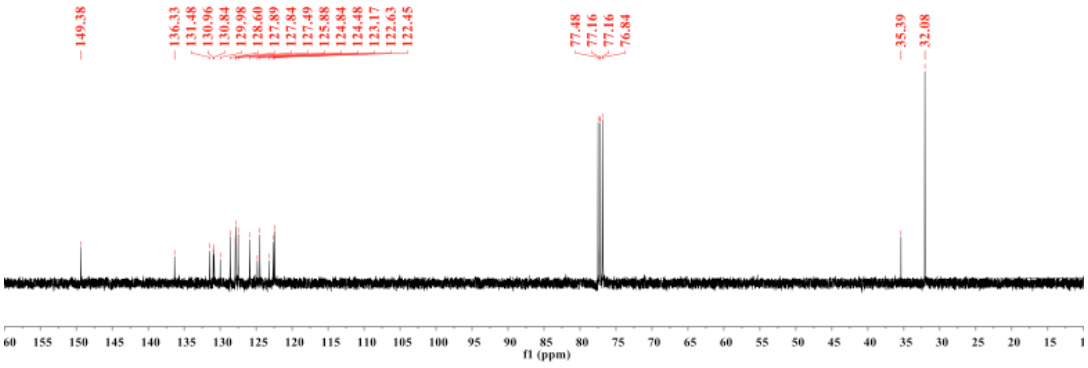

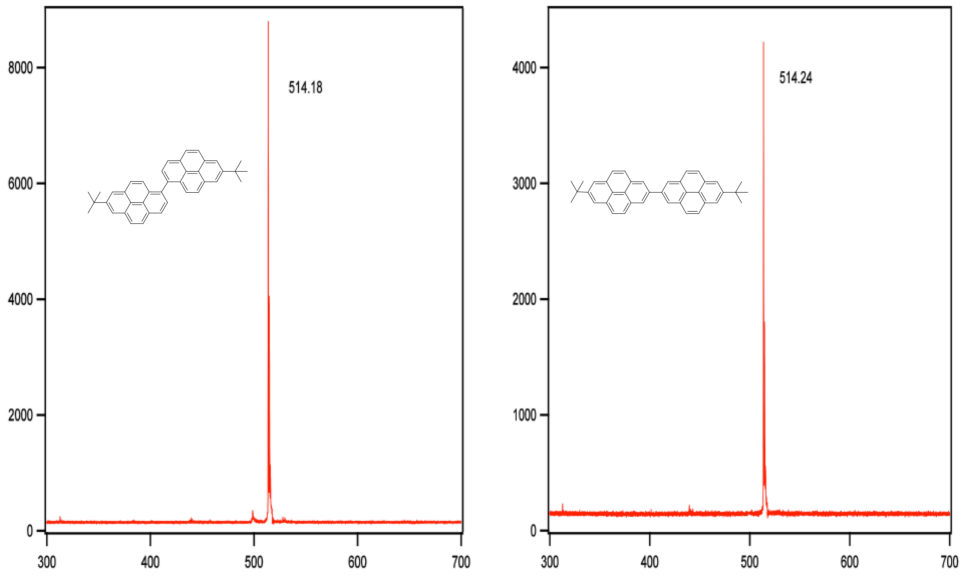

Figure S4. MALDI spectra of the tert-butylated pyrenes

Electrochemistry

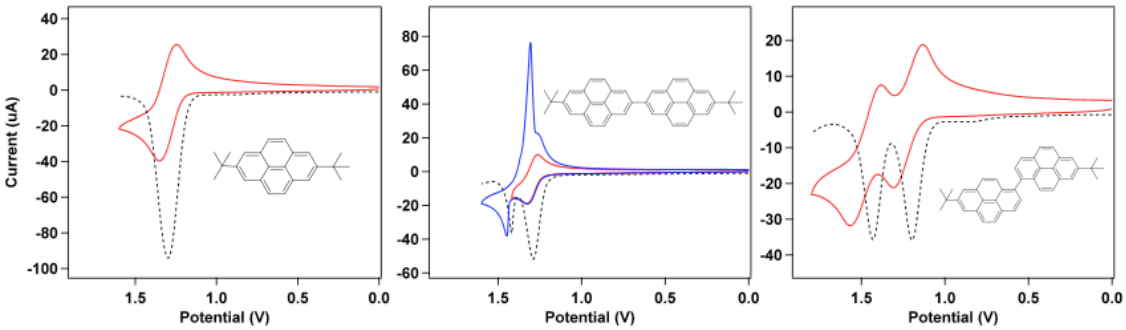

Figure S5. Cyclic voltammograms and square waves of 2,7-tBu-pyrene, *para*-tBu-bipyrene, *meta*-tBu-bipyrene.

Table S3. Oxidation potentials of the tert-butylated pyrenes

	E_{ox1}	E_{ox2}
2,7-tBu-pyrene	0.83	
para-tBu-bipyrene	0.82	0.95
meta-tBu-bipyrene	0.76	0.99
2-tBu-pyrene	0.84	1.0

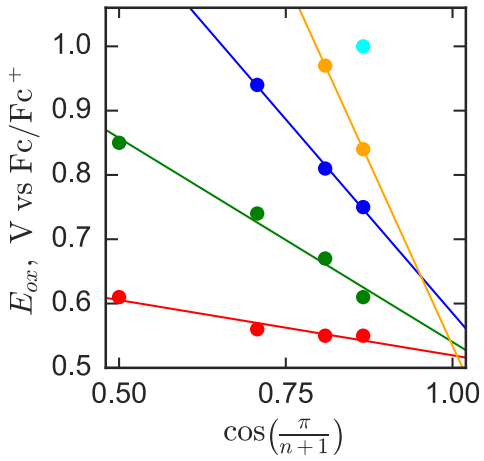

Figure S6. Plot of the Experimental first (red), second (green), third (blue), forth (orange) and fifth (cyan) oxidation potentials (V vs Fc/Fc$^+$) of *m*-**Py**$_n$ (n = 1-5) against cos[π/(n+1)] trend.

Table S4. Experimental first, second, third, forth and fifth oxidation potentials (V vs Fc/Fc$^+$) of **Py**$_n$ (n = 1-5).

n	E_{ox1}	E_{ox2}	E_{ox3}	E_{ox4}	E_{ox5}
1	0.67				
2	0.61	0.85			
3	0.56	0.74	0.94		
4	0.55	0.67	0.81	0.97	
5	0.55	0.61	0.75	0.84	1.00

S2. Generation of $\mathbf{Py}_n^{+\bullet}$ by redox titrations

The reproducible spectra of cation radicals of *m*-$\mathbf{Py}_n$ in CH_2Cl_2 at 22 ºC were obtained by quantitative redox titrations using three different aromatic oxidants, i.e. [$\mathbf{THEO}^{+\bullet}SbCl_6^-$] ($E_{red1}$ = 0.67 V vs Fc/Fc^+, λ_{max} = 518 nm, ε_{max} = 7300 cm^{-1} M^{-1}),[3] [$\mathbf{NAP}^{+\bullet}SbCl_6^-$] ($E_{red1}$ = 0.94 V vs Fc/Fc^+, λ_{max} = 672 nm, ε_{max} = 9300 cm^{-1} M^{-1})[4-6] and $\mathbf{ANT}^{+\bullet}$ (E_{red1} = 0.53 V vs Fc/Fc^+, λ_{max} = 744 nm, ε_{max} = 23400 cm^{-1} M^{-1}) obtained via redox titration with $\mathbf{NAP}^{+\bullet}$ (Figure S7).

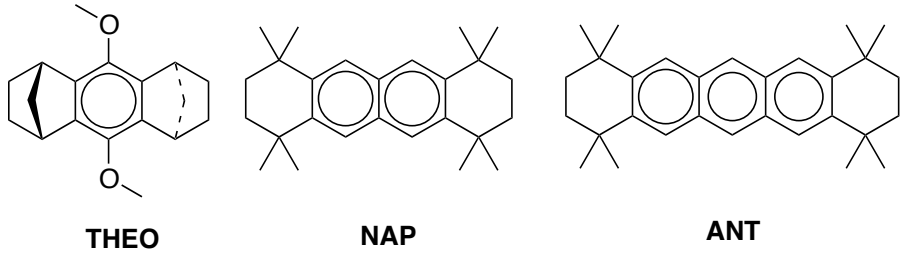

Figure S7. Chemical structures and names of three aromatic oxidants used in redox titrations.

Each redox titration experiment was carried out by an incremental addition of sub-stoichiometric amounts of electron donor (*m*-$\mathbf{Py}_n$) to the solution of an oxidant cation radical ($\mathbf{Ox}^{+\bullet}$). The 1-e^- oxidation of *m*-$\mathbf{Py}_n$ to *m*-$\mathbf{Py}_n^{+\bullet}$ and reduction of $\mathbf{Ox}^{+\bullet}$ to **Ox** can be described by an equilibrium shown in eq. 1.

$$\mathbf{Ox}^{+\bullet} + m\text{-}\mathbf{Py}_n \rightleftarrows \mathbf{Ox} + m\text{-}\mathbf{Py}_n^{+\bullet} \qquad \text{(eq. 1)}$$

The redox titrations with two successive 1-e^- oxidations involve multiple equilibria: one- and two-electron redox reactions between the donor and oxidant (eqs. 2 and 3) and comproportionation/disproportionation of $\mathbf{D}^{2+}/\mathbf{D}^{+\bullet}$ (eq. 4).

$$\mathbf{Ox}^{+\bullet} + \mathbf{D} \overset{K_1}{\rightleftarrows} \mathbf{Ox} + \mathbf{D}^{+\bullet} \qquad \text{(eq. 2)}$$

$$\mathbf{Ox}^{+\bullet} + \mathbf{D}^{+\bullet} \overset{K_2}{\rightleftarrows} \mathbf{Ox} + \mathbf{D}^{2+} \qquad \text{(eq. 3)}$$

$$\mathbf{D}^{2+} + \mathbf{D} \overset{K_3}{\rightleftarrows} 2\mathbf{D}^{+\bullet} \qquad \text{(eq. 4)}$$

Numerical deconvolution of the absorption spectrum at each increment (Figures S9-S22, left) produced mole fractions of each species ($\mathbf{Ox}^{+\bullet}$ and *m*-$\mathbf{Py}_n^{+\bullet}$ and/or *m*-$\mathbf{Py}_n^{2+}$) against the added equivalents of $\mathbf{Py}_n$ (Figures S9-S22, right), confirming a 1:1 stoichiometry of each redox reaction. The experimental points of mole fraction vs equivalent of added donor *m*-$\mathbf{Py}_n$ were fitted by varying ΔG_1 ($= E_{ox1}^{\mathbf{Py}n} - E_{red}^{\mathbf{Ox}^{+\bullet}}$) and ΔG_{12} ($= E_{ox2}^{\mathbf{Py}n} - E_{ox1}^{\mathbf{Py}n}$).[7,8]

Table S5. Values of ΔG_1 and ΔG_{12} obtained by fitting to the experimental mole fraction plots (Figures S9-S25).[7,8]

n	**ANT**$^{+\bullet}$ + *m*-**Py**$_n$	**THEO**$^{+\bullet}$ + *m*-**Py**$_n$	**NAP**$^{+\bullet}$ + *m*-**Py**$_n$	
	ΔG_1, meV	ΔG_1, meV	ΔG_1, meV	ΔG_{12}, meV
1	65	30	-176	--
2	26	-116	-253	229
3	-4	-146	-266	169
4	-9	-144	--	--
5	-22	-131	--	--

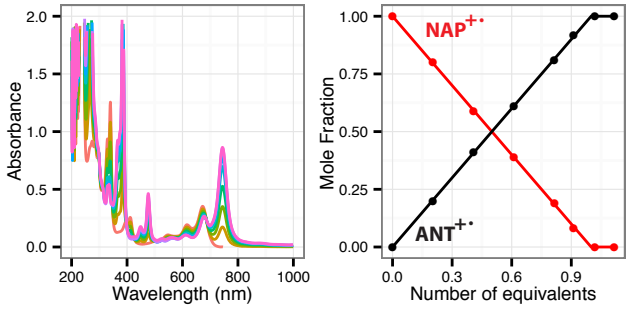

Figure S8. Left: Spectral changes observed upon the reduction of 0.038 mM **NAP**$^{+\bullet}$ in CH_2Cl_2 (3 mL) by addition of 15-µL increments of 2.38 mM solution of **ANT** in CH_2Cl_2. **Right**: Plot of the mole fractions of **NAP**$^{+\bullet}$ (red) and **ANT**$^{+\bullet}$ (black) against the added equivalents of **ANT**. Symbols represent experimental points, while the solid lines show best-fit to the experimental points using ΔG_1 = -1.3 eV.

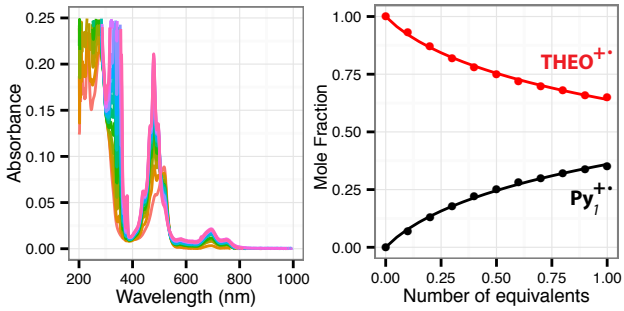

Figure S9. Left: Spectral changes observed upon the reduction of 0.012 mM **THEO**$^{+\bullet}$ in CH_2Cl_2 (3 mL) by addition of 15-µL increments of 1.45 mM solution of $\mathbf{Py_1}$ in CH_2Cl_2. **Right**: Plot of the mole fractions of **THEO**$^{+\bullet}$ (red) and $\mathbf{Py_1}^{+\bullet}$ (black) against the added equivalents of $\mathbf{Py_1}$. Symbols represent experimental points, while the solid lines show best-fit to the experimental points using $\Delta G_1 = 30$ meV.

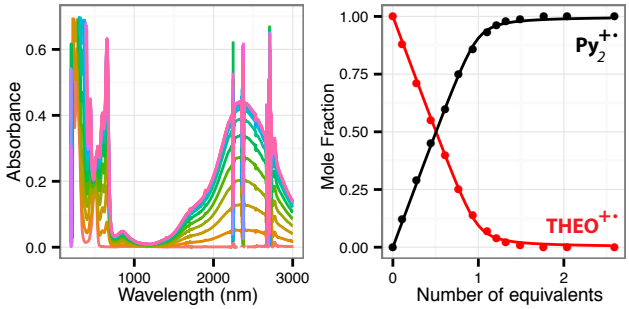

Figure S10. Left: Spectral changes observed upon the reduction of 0.031 mM **THEO**$^{+\bullet}$ in CH_2Cl_2 (3 mL) by addition of 15-µL increments of 0.86 mM solution of $\mathbf{Py_2}$ in CH_2Cl_2. **Right**: Plot of the mole fractions of **THEO**$^{+\bullet}$ (red) and $\mathbf{Py_2}^{+\bullet}$ (black) against the added equivalents of $\mathbf{Py_2}$. Symbols represent experimental points, while the solid lines show best-fit to the experimental points using $\Delta G_1 = -116$ meV.

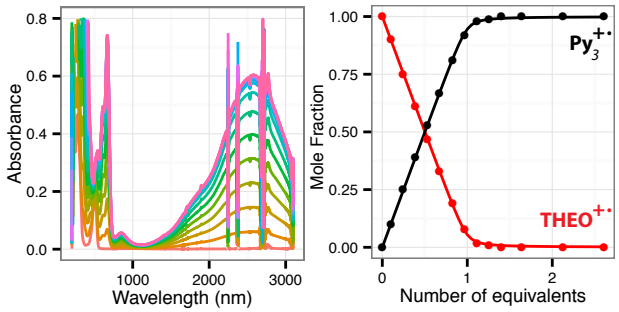

Figure S11. Left: Spectral changes observed upon the reduction of 0.029 mM **THEO**$^{+\bullet}$ in CH_2Cl_2 (3 mL) by addition of 15-µL increments of 0.76 mM solution of $\mathbf{Py_3}$ in CH_2Cl_2. **Right**: Plot of the mole fractions of **THEO**$^{+\bullet}$ (red) and $\mathbf{Py_3}^{+\bullet}$ (black) against the added equivalents of $\mathbf{Py_3}$. Symbols represent experimental points, while the solid lines show best-fit to the experimental points using $\Delta G_1 = -146$ meV.

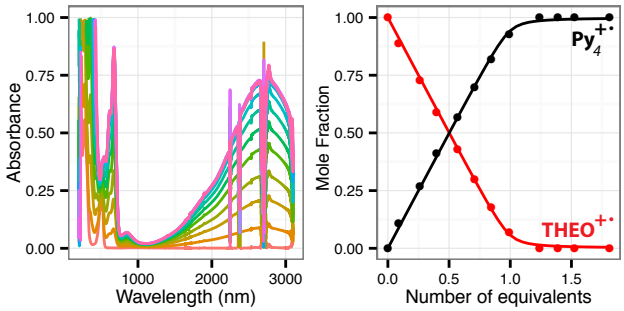

Figure S12. Left: Spectral changes observed upon the reduction of 0.035 mM **THEO**$^{+\bullet}$ in CH_2Cl_2 (3 mL) by addition of 15-µL increments of 0.48 mM solution of **Py$_4$** in CH_2Cl_2. **Right**: Plot of the mole fractions of **THEO**$^{+\bullet}$ (red) and **Py$_4$**$^{+\bullet}$ (black) against the added equivalents of **Py$_4$**. Symbols represent experimental points, while the solid lines show best-fit to the experimental points using ΔG_1 = -144 meV.

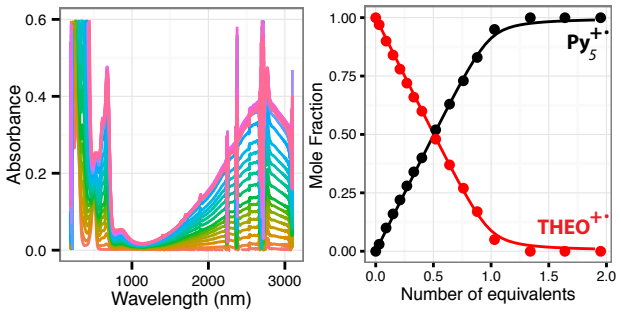

Figure S13. Left: Spectral changes observed upon the reduction of 0.022 mM **THEO**$^{+\bullet}$ in CH_2Cl_2 (3 mL) by addition of 15-µL increments of 0.41 mM solution of **Py$_5$** in CH_2Cl_2. **Right**: Plot of the mole fractions of **THEO**$^{+\bullet}$ (red) and **Py$_5$**$^{+\bullet}$ (black) against the added equivalents of **Py$_5$**. Symbols represent experimental points, while the solid lines show best-fit to the experimental points using ΔG_1 = -131 meV.

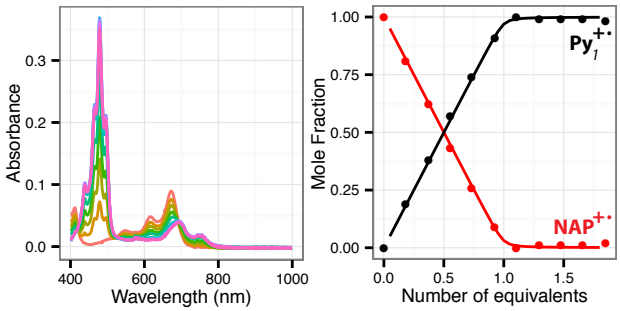

Figure S14. Left: Spectral changes observed upon the reduction of 0.0097 mM **NAP**$^{+\bullet}$ in CH_2Cl_2 (3 mL) by addition of 15-µL increments of 2.23 mM solution of **Py$_1$** in CH_2Cl_2. **Right**: Plot of the mole fractions of **NAP**$^{+\bullet}$ (red) and **Py$_1$**$^{+\bullet}$ (black) against the added equivalents of **Py$_1$**. Symbols represent experimental points, while the solid lines show best-fit to the experimental points using ΔG_1 = -176 meV.

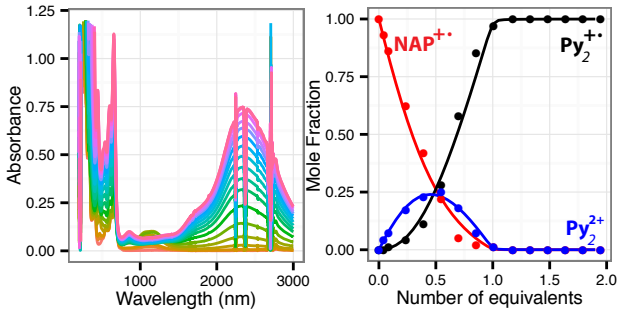

Figure S15. Left: Spectral changes observed upon the reduction of 0.041 mM **NAP**$^{+\bullet}$ in CH_2Cl_2 (3 mL) by addition of 15-µL increments of 1.39 mM solution of **Py$_2$** in CH_2Cl_2. **Right**: Plot of the mole fractions of **NAP**$^{+\bullet}$ (red), **Py$_2$**$^{+\bullet}$ (black) and **Py$_2$**$^{2+}$ (blue) against the added equivalents of **Py$_2$**. Symbols represent experimental points, while the solid lines show best-fit to the experimental points using ΔG_1 = -253 meV and ΔG_{12} = 229 meV.

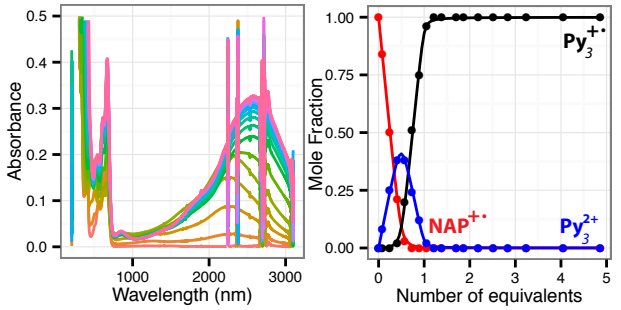

Figure S16. Left: Spectral changes observed upon the reduction of 0.033 mM **NAP**$^{+\bullet}$ in CH_2Cl_2 (3 mL) by addition of 15-µL increments of 1.18 mM solution of **Py$_3$** in CH_2Cl_2. **Right**: Plot of the mole fractions of **NAP**$^{+\bullet}$ (red), **Py$_3$**$^{+\bullet}$ (black) and **Py$_3$**$^{2+}$ (blue) against the added equivalents of **Py$_3$**. Symbols represent experimental points, while the solid lines show best-fit to the experimental points using ΔG_1 = -266 meV and ΔG_{12} = 169 meV.

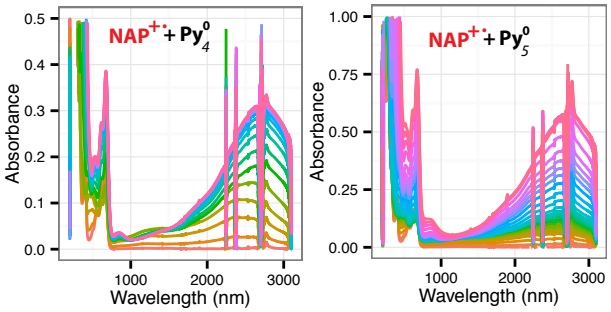

Figure S17. Left: Spectral changes observed upon the reduction of 0.028 mM **NAP**$^{+\bullet}$ in CH_2Cl_2 (3 mL) by addition of 15-µL increments of 0.60 mM solution of **Py$_4$** in CH_2Cl_2. **Right**: Spectral changes observed upon the reduction of 0.032 mM **NAP**$^{+\bullet}$ in CH_2Cl_2 (3 mL) by addition of 15-µL increments of 0.53 mM solution of **Py$_5$** in CH_2Cl_2.

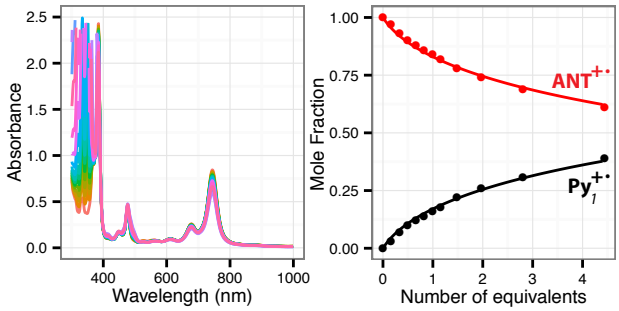

Figure S18. Left: Spectral changes observed upon the reduction of 0.036 mM **ANT**$^{+\bullet}$ in CH_2Cl_2 (3 mL) by addition of 15-µL increments of 1.78 mM solution of $\mathbf{Py_1}$ in CH_2Cl_2. **Right**: Plot of the mole fractions of **ANT**$^{+\bullet}$ (red) and $\mathbf{Py_1}^{+\bullet}$ (black) against the added equivalents of $\mathbf{Py_1}$. Symbols represent experimental points, while the solid lines show best-fit to the experimental points using ΔG_1 = 65 mV.

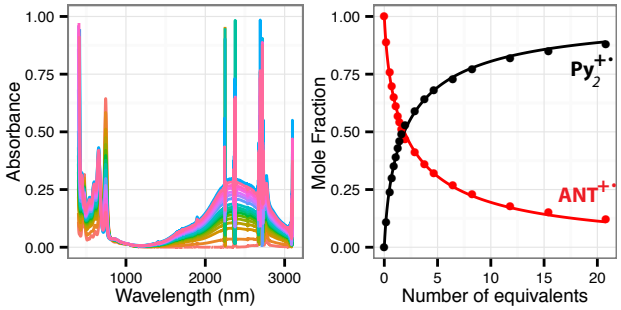

Figure S19. Left: Spectral changes observed upon the reduction of 0.028 mM **ANT**$^{+\bullet}$ in CH_2Cl_2 (3 mL) by addition of 15-µL increments of 1.14 mM solution of $\mathbf{Py_2}$ in CH_2Cl_2. **Right**: Plot of the mole fractions of **ANT**$^{+\bullet}$ (red) and $\mathbf{Py_2}^{+\bullet}$ (black) against the added equivalents of $\mathbf{Py_1}$. Symbols represent experimental points, while the solid lines show best-fit to the experimental points using ΔG_1 = 26 mV.

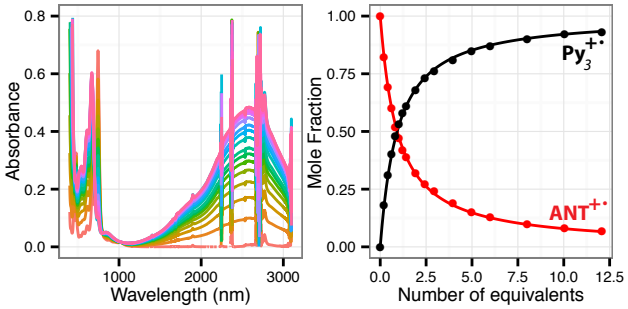

Figure S20. Left: Spectral changes observed upon the reduction of 0.029 mM **ANT**$^{+\bullet}$ in CH_2Cl_2 (3 mL) by addition of 15-µL increments of 0.74 mM solution of $\mathbf{Py_3}$ in CH_2Cl_2. **Right**: Plot of the mole fractions of **ANT**$^{+\bullet}$ (red) and $\mathbf{Py_3}^{+\bullet}$ (black) against the added equivalents of $\mathbf{Py_3}$. Symbols represent experimental points, while the solid lines show best-fit to the experimental points using ΔG_1 = -4 mV.

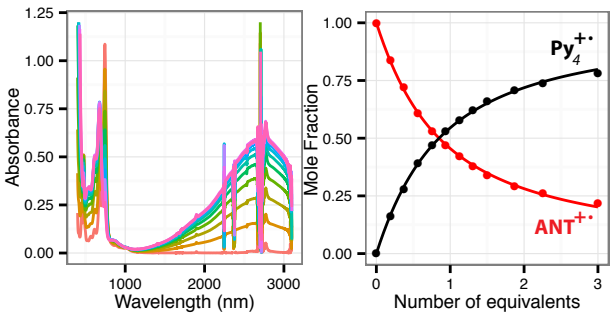

Figure S21. Left: Spectral changes observed upon the reduction of 0.046 mM **ANT**$^{+\bullet}$ in CH_2Cl_2 (3 mL) by addition of 15-µL increments of 0.44 mM solution of **Py$_4$** in CH_2Cl_2. **Right**: Plot of the mole fractions of **ANT**$^{+\bullet}$ (red) and **Py$_4$**$^{+\bullet}$ (black) against the added equivalents of **Py$_4$**. Symbols represent experimental points, while the solid lines show best-fit to the experimental points using ΔG_1 = -9 mV.

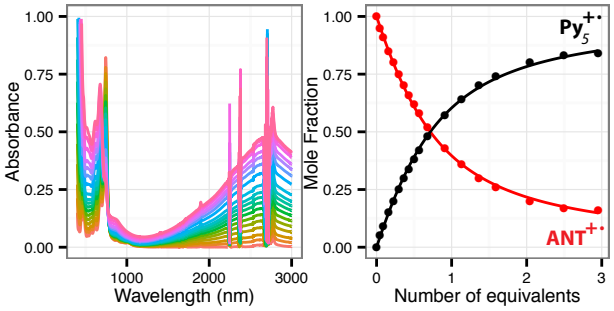

Figure S22. Left: Spectral changes observed upon the reduction of 0.035 mM **ANT**$^{+\bullet}$ in CH_2Cl_2 (3 mL) by addition of 15-µL increments of 0.26 mM solution of **Py$_5$** in CH_2Cl_2. **Right**: Plot of the mole fractions of **ANT**$^{+\bullet}$ (red) and **Py$_5$**$^{+\bullet}$ (black) against the added equivalents of **Py$_5$**. Symbols represent experimental points, while the solid lines show best-fit to the experimental points using ΔG_1 = -22 mV.

Density functional theory calculations

Computational details

The electronic structure calculations were performed using B1LYP-40/6-31G(d)[9,10] level of theory with 40% contribution of the Hartree-Fock exchange term[11-15] as implemented in Gaussian 09 package, revision D.01.[16] Solvent effects were included using the implicit integral equation formalism polarizable continuum model (IEF-PCM)[17-21] with dichloromethane solvent parameters (ε = 8.93). Ultrafine Lebedev's grid was used with 99 radial shells per atom and 590 angular points in each shell. Tight cutoffs on forces and atomic displacement were used to determine convergence in geometry optimization procedure. Harmonic vibrational frequency calculations were performed for the optimized $\mathbf{Py}_n$/$\mathbf{Py}_n^{+\bullet}$ (n = 1-4) structures to confirm absence of imaginary frequencies. The transition state of m-$\mathbf{Py}_4^{+\bullet}$ was confirmed by the presence of a single imaginary frequency (i549.6) and IRC calculations[22] that led to expected equilibrium geometries of m-$\mathbf{Py}_4^{+\bullet}$.

For cation radicals, wavefunction stability tests[23] were performed to ensure absence of solutions with lower energy. The values of $\langle S^2 \rangle$ operator after spin annihilation were confirmed to be close to the expectation value of 0.75. Unpaired spin density surface were obtained using isovalue of 0.001 a.u. Atomic charges were calculated using natural population analysis approach.[24,25] Calculations of the first excited state of $\mathbf{Py}_n$ and $\mathbf{Py}_n^{+\bullet}$ were performed using the time-dependent density functional theory (TD-DFT) method.[26-30]

S3. *m*-Py$_n$ in neutral and cation radical states

Table S6. Energies (ν) and oscillator strength (f_{osc}) of $S_0 \rightarrow S_1$ transitions, oxidation energies (E_{ox1}) of *m*-**Py**$_n$, energies (ν) and oscillator strengths (f_{osc}) of $D_0 \rightarrow D_1$ transitions in *m*-**Py**$_n^{+\bullet}$ calculated using (TD) B1LYP-40/6-31G(d)+PCM(CH_2Cl_2).

	m-**Py**$_n$ absorption $S_0 \rightarrow S_1$			*m*-**Py**$_n^{+\bullet}$ absorption $D_0 \rightarrow D_1$			E_{ox1}, eV
n	ν, eV	λ, nm	f_{osc}	ν, eV	λ, nm	f_{osc}	
1	3.78	328	0.571	1.54	807	0.000	5.14
2	3.48	356	1.030	0.59	2096	0.353	5.03
3	3.34	371	1.697	0.67	1861	0.466	4.98
4	3.29	377	2.400	0.62	2010	0.541	4.99
5	3.25	381	3.131	0.60	2081	0.626	4.99
6	3.23	383	3.846	0.59	2098	0.647	4.99
7	3.22	385	4.584	0.59	2093	0.665	4.99

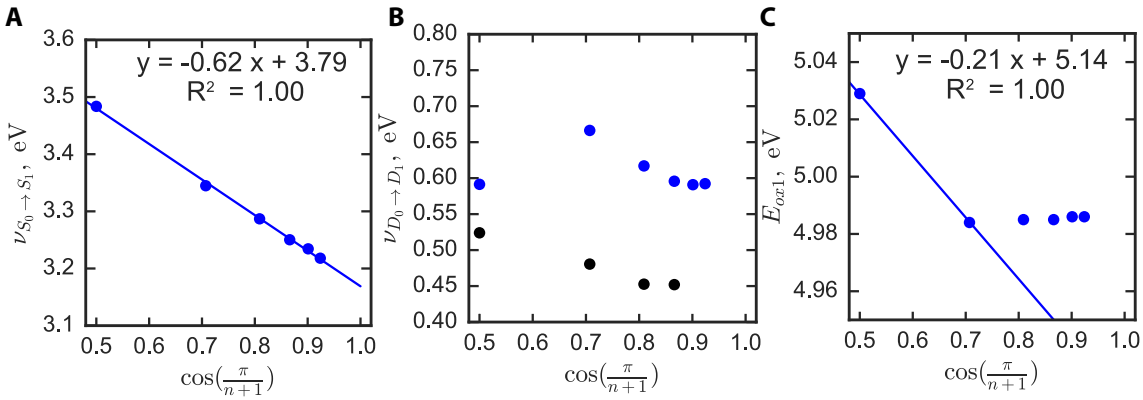

Figure S23. Plots of $S_0 \rightarrow S_1$ excitation energies of *m*-**Py**$_n$ (**A**), $D_0 \rightarrow D_1$ excitation energies of *m*-**Py**$_n^{+\bullet}$ (**B**; blue: DFT, black: experiment) and first oxidation energies E_{ox1} of *m*-**Py**$_n$ against cos[π/(*n*+1)] calculated using (TD) B1LYP-40/6-31G(d)+PCM(CH_2Cl_2) level of theory.

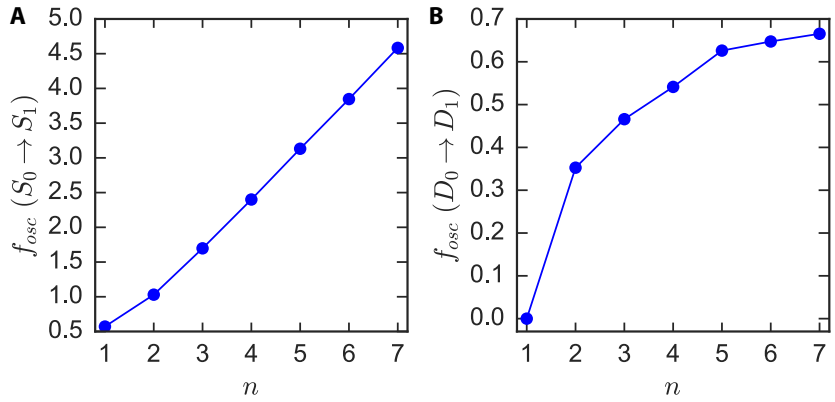

Figure S24. Oscillators strengths (f_{osc}) of $S_0 \rightarrow S_1$ transitions in *m*-**Py**$_n$, *n* = 1-7 (**A**) and $D_0 \rightarrow D_1$ transitions in *m*-**Py**$_n^{+\bullet}$, *n* = 1-7 (**B**)

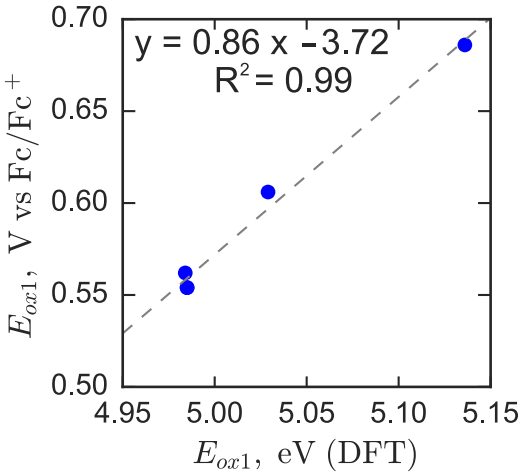

Figure S25. Correlation plot between experimental first oxidation potential E_{ox1} (V vs Fc/Fc$^+$) and first oxidation energies E_{ox1} (eV) calculated at B1LYP-40/6-31G(d)+PCM(CH_2Cl_2) level of theory.

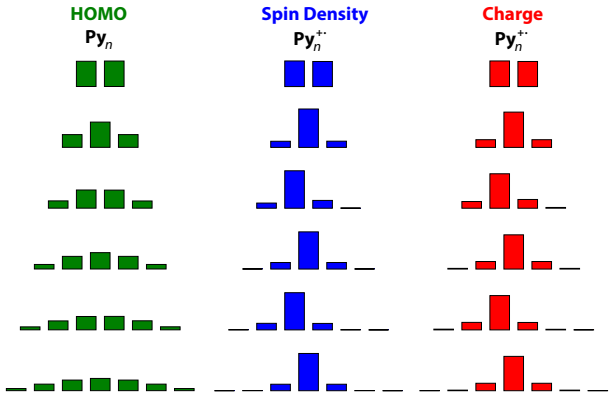

Figure S26. Per-unit barplot representations of HOMOs of neutral *m*-**Py**$_n$, NPA spin densities and charges of *m*-**Py**$_n^{+\bullet}$ in ground state.

Table S7. Comparison of the oxidation-induced bond length changes in the tetraisopropylpyrene (**TIP**) obtained from X-ray crystallography and from calculations using B1LYP-40/6-31G(d)+PCM(CH_2Cl_2).[31]

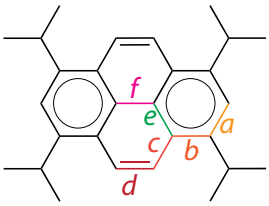

	DFT (**TIP**), pm	DFT (**TIP**$^{+\bullet}$), pm	Δ DFT, pm	Δ X-Ray, pm
a	139.0	138.85	-0.15	-0.3
b	141.0	143.3	2.3	2.4
c	143.4	140.8	-2.6	-2.2
d	135.1	137.4	2.3	2.8
e	142.6	142.3	-0.3	-0.3
f	143.8	142.5	-1.3	-1.8

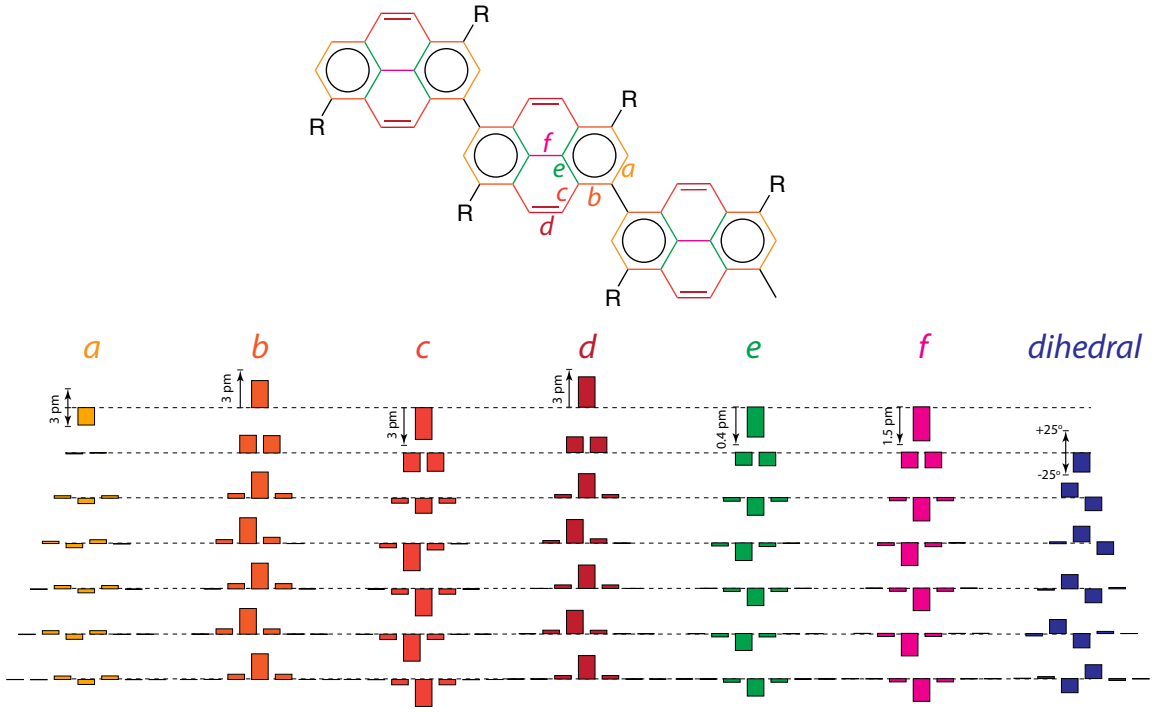

Figure S27. Distribution of the oxidation-induced bond lengths and dihedral angle changes in *m*-**Py**$_n$/*m*-**Py**$_n^{+\bullet}$ calculated using B1LYP-40/6-31G(d)+PCM(CH_2Cl_2).

Table S8. Energy (electronic energy *E*, enthalpy *H* and free energy *G*) differences between transition state and equilibrium structures of *m*-**Py**$_4^{+\bullet}$ and a value of the imaginary frequency of the transition state. Mode displacements with the imaginary frequencies are represented by vectors below.

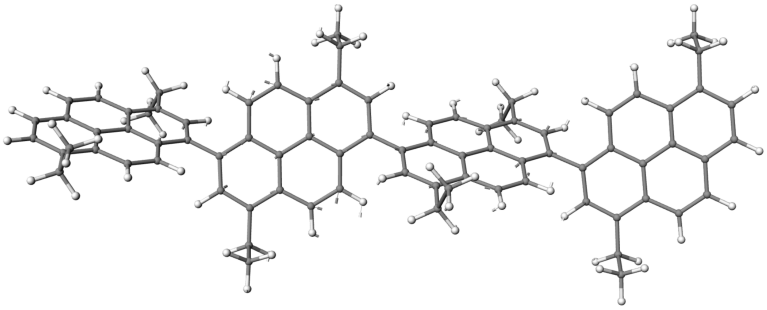

ω, cm^{-1}	$\Delta E^{\ddagger}$, kcal/mol	$\Delta H^{\ddagger}$, kcal/mol	$\Delta G^{\ddagger}$, kcal/mol
i549.6	0.19	-1.48	-1.01

S4. *p*-Py$_n$ in neutral and cation radical states

Table S9. Energies (ν) and oscillator strength (f_{osc}) of $S_0 \rightarrow S_1$ transitions, oxidation energies (E_{ox1}) of *p*-**Py**$_n$, energies (ν) and oscillator strengths (f_{osc}) of $D_0 \rightarrow D_1$ transitions in *p*-**Py**$_n^{+\bullet}$ calculated using (TD) B1LYP-40/6-31G(d)+PCM(CH_2Cl_2).

	p-**Py**$_n$ absorption $S_0 \rightarrow S_1$			*p*-**Py**$_n^{+\bullet}$ absorption $D_0 \rightarrow D_1$			E_{ox1}, eV
n	ν, eV	λ, nm	f_{osc}	ν, eV	λ, nm	f_{osc}	
1	3.78	328	0.571	1.54	807	0.000	5.14
2	3.68	337	1.414	0.75	1648	0.004	5.15
3	3.63	341	2.389	0.72	1729	0.008	5.18
4	3.61	343	3.427	0.72	1733	0.005	5.18
5	3.60	344	4.381				5.18

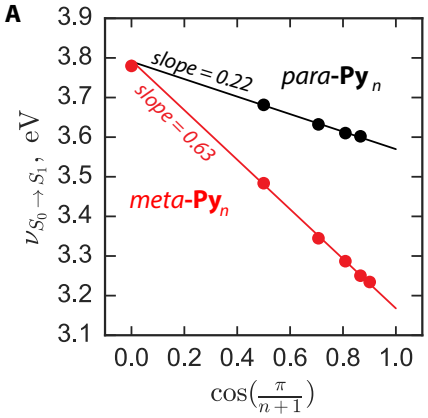

Figure S28. Evolution of the $S_0 \rightarrow S_1$ transition energies in *p*-**Py**$_n$ and *m*-**Py**$_n$ against cos[π/(*n*+1)] trend calculated using TD-B1LYP-40/6-31G(d)+PCM(CH_2Cl_2).

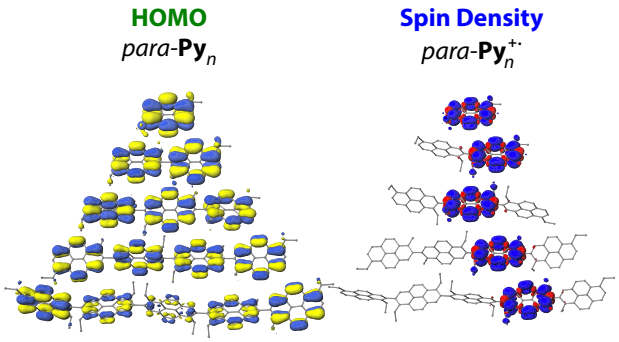

Figure S29. Isovalue plots of HOMOs (0.03 au) of neutral *p*-**Py**$_n$ and spin-densities (0.001 au) of *p*-**Py**$_n^{+\bullet}$ calculated using B1LYP-40/6-31G(d)+PCM(CH_2Cl_2).

Theoretical Modeling

S5. Marcus-Hush two-state models of $F_2^{+\bullet}$, *m*-$Py_2^{+\bullet}$ and *p*-$Py_2^{+\bullet}$

To investigate the mechanism of hole stabilization in $\mathbf{F_2}^{+\bullet}$, *m*-$\mathbf{Py_2}^{+\bullet}$ and *p*-$\mathbf{Py_2}^{+\bullet}$ we performed the computational scans, obtained as series of constrained optimizations with fixed interchromophoric dihedral angle (ϕ = 0°-90° at 5° increment) and subsequent single point TD-DFT calculation of the excitation energy (ν), as shown schematically in Figure S30B.[32]

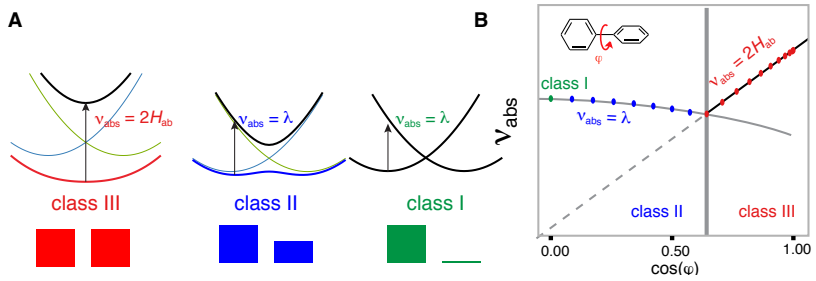

Figure S30. (A) Robin-Day classification of the mixed-valence compounds. (B) A schematic plot of ν against cos(φ). Two distinct regions are separated by the crossover angle, where mechanism of hole delocalization changes from full delocalization (class III) to partial delocalization (class II)

As the electronic coupling H_{ab} scales linearly with cos(φ), the computed ν follows a linear dependence with cos(φ) in the range of angles where $\nu = 2H_{ab}$, $2H_{ab} > \lambda$ (Figure S30B). While the electronic coupling H_{ab} continues to decrease linearly with lowering of cos(φ), in case when $2H_{ab}$ equals λ, hole delocalization switches to a different regime with the ν-vs-cos(φ) dependence that is among various polynomials is best described by the quadratic function (Figure S30B). This switch in the ν/cos(φ) dependence corresponds to the change in the mechanism of hole delocalization from full delocalization(class III) to partial delocalization (class II). Based on the Marcus-Hush two-state model in case of $2H_{ab} < \lambda$, the energy ν directly provides the value of reorganization energy, i.e. $\nu = \lambda$.[33]

Table S10. Linear and quadratic trends fitted to the data points from computational scans of *m*-$\mathbf{Py_2}^{+\bullet}$ and $\mathbf{F_2}^{+\bullet}$

	$\nu_{abs} = 2H_{ab}$	$\nu_{abs} = \lambda$	H_{ab}, eV	λ, eV
$\mathbf{F_2}^{+\bullet}$	$y = 1.00x + 0.25$	$y = -0.69x^2 + 0.12x + 0.83$	0.60	0.33
m-$\mathbf{Py_2}^{+\bullet}$	$y = 1.01x - 0.06$	$y = -0.31x^2 + 0.05x + 0.66$	0.30	0.56

S6. Application of multistate state model (MSM) to *m*-Py$_n^{+\bullet}$

Complete oxidation of the pyrene unit with coordinate x_i leads to the structural distortions of this unit and accumulation of the negative charge from the solvent around the unit. Then, with the geometry of the wire and solvent arrangement being fixed, a variation of the reaction coordinate *x* in the vicinity of the reorganized unit leads to the quadratic increase in energy, while at a larger separation distance (i.e. $x - x_i$) the energy reaches a finite value following the Coulomb law of the electrostatic interaction.[34] The diabatic state $H_i(x)$ can be represented as a bell-shaped continuous function of the charge coordinate x using the composite quadratic/reciprocal dependence:[34]

$$H_i(x) = \begin{cases} \lambda(x - x_i)^2, & if\ |x - x_i| \le t \\ \lambda^\infty - a/|x - x_i|, & if\ |x - x_i| \ge t \end{cases}$$

where λ is the structural reorganization, λ^∞ is the energy of the completely separated hole and reorganization, parameters $t = \sqrt{\lambda^\infty/3\lambda}$ and $a = 2\lambda t^3$ are defined by the continuity of $H_i(x)$ and its first derivative. Parameter t defines a separation distance after which the interaction mechanism switches from the short-range to the long-range interaction.

The Hamiltonian matrix can be represented as:

$$\mathbf{H}(x) = \begin{bmatrix} H_1(x) & H_{\mathrm{ab}} & \cdots & 0 & 0 \\ H_{\mathrm{ab}} & H_2(x) & \cdots & 0 & 0 \\ \vdots & \vdots & \ddots & \vdots & \vdots \\ 0 & 0 & \cdots & H_{n-1}(x) & H_{\mathrm{ab}} \\ 0 & 0 & \cdots & H_{\mathrm{ab}} & H_n(x) \end{bmatrix}$$

Hamiltonian matrices at various x were constructed using values H_{ab} = 0.33 eV and λ = 0.56 eV obtained from the computational scan, and $\lambda^\infty = 3.5\ eV$ obtained via empirical adjustment to reproduce excitation energies.[34] Numerical diagonalization of the Hamiltonian matrix $\mathbf{H}(x)$ for each x results in the adiabatic potential energy surface with the lowest-energy surface $G_0(x)$ corresponding to the ground state of **Py**$_n^{+\bullet}$. The minimum on the ground state surface $G_0(x)$ defines the position x_{min} of the center of the hole distribution and the lowest energy eigenvalue at this point $G_0(x_{min})$ corresponds to the oxidation potential E_{ox1} of **Py**$_n$. The difference between two lowest eigenvalues at point x_{min} provides the vertical excitation energy, i.e. $\Delta G(x_{\mathrm{min}}) = G_1(x_{\mathrm{min}}) - G_0(x_{\mathrm{min}})$.

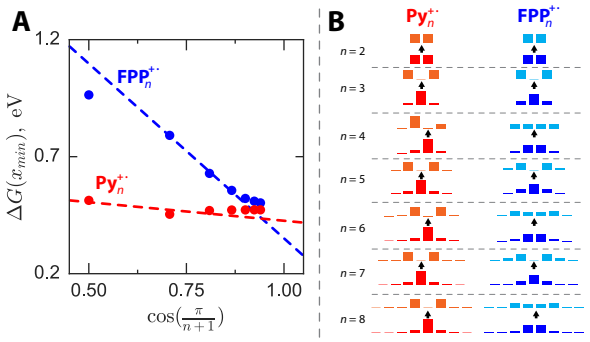

Figure S31. A: Plot of excitation energies of *m*-$\mathbf{Py}_n^{+\bullet}$ and $\mathbf{F}_n^{+\bullet}$ from MSM. **B**: Barplot representation of the hole of *m*-$\mathbf{Py}_n^{+\bullet}$ and $\mathbf{F}_n^{+\bullet}$ in the ground and vertically excited state from MSM.

References

(1) Bédard, A. -C.; Vlassova, A.; Hernandez-Perez, A. C.; Bessette, A.; Hanan, G. S.; Heuft, M. A.; Collins, S. K. Synthesis, Crystal Structure and Photophysical Properties of Pyrene--helicene Hybrids. *Chem. Eur. J.* **2013**, *19*, 16295-16302.
(2) Figueira-Duarte, T. M.; Simon, S. C.; Wagner, M.; Druzhinin, S. I.; Zachariasse, K. A.; Müllen, K. Polypyrene Dendrimers. *Angew. Chem. Int. Ed. Engl.* **2008**, *47*, 10175-10178.
(3) Rathore, R.; Burns, C. L.; Deselnicu, M. I. Preparation of 1, 4: 5, 8-Dimethano-1, 2, 3, 4, 5, 6, 7, 8-Octahydro-9, 10-Dimethoxyanthracenium Hexachloroantimonate (4+ SbCl6-): A Highly Robust Radical-Cation Salt. *Org. Synth.* **2005**, 1-9.
(4) Rathore, R.; Kochi, J. K. Acid Catalysis Vs. Electron-transfer Catalysis Via Organic Cations or Cation-radicals As the Reactive Intermediate. Are These Distinctive Mechanisms? *Acta. Chem. Scand.* **1998**, *52*, 114-130.
(5) Rathore, R.; Burns, C. L.; Deselnicu, M. I. Multiple-electron Transfer in a Single Step. Design and Synthesis of Highly Charged Cation-radical Salts. *Org. Lett.* **2001**, *3*, 2887-2890.
(6) Rathore, R.; Kochi, J. K. Acid Catalysis Vs. Electron-transfer Catalysis Via Organic Cations or Cation-radicals As the Reactive Intermediate. Are These Distinctive Mechanisms? *Acta. Chem. Scand.* **1998**, *52*, 114-130.
(7) Talipov, M. R.; Boddeda, A.; Hossain, M. M.; Rathore, R. Quantitative Generation of Cation Radicals and Dications Using Aromatic Oxidants: Effect of Added Electrolyte on the Redox Potentials of Aromatic Electron Donors. *J. Phys. Org. Chem.* **2015**, *29*, 227-233.
(8) Talipov, M. R.; Hossain, M. M.; Boddeda, A.; Thakur, K.; Rathore, R. A Search for Blues Brothers: X-ray Crystallographic/spectroscopic Characterization of the Tetraarylbenzidine Cation Radical As a Product of Aging of Solid Magic Blue. *Org. Biomol. Chem.* **2016**, *14*, 2961-2968.
(9) Hehre, W. J.; Ditchfield, R.; Pople, J. A. Selfconsistent Molecular Orbital Methods. XII. Further Extensions of Gaussiantype Basis Sets for Use in Molecular Orbital Studies of Organic Molecules. *J. Chem. Phys.* **1972**, *56*, 2257-2261.
(10) Adamo, C.; Barone, V. Toward Reliable Adiabatic Connection Models Free From Adjustable Parameters. *Chem. Phys. Lett.* **1997**, *274*, 242-250.
(11) Félix, M.; Voityuk, A. A. DFT Performance for the Hole Transfer Parameters in DNA Π Stacks. *Int. J. Quantum. Chem.* **2011**, *111*, 191-201.
(12) Dierksen, M.; Grimme, S. The Vibronic Structure of Electronic Absorption Spectra of Large Molecules: A Time-dependent Density Functional Study on the Influence of Exact Hartree-Fock Exchange. *J. Phys. Chem. A.* **2004**, *108*, 10225-10237.
(13) Talipov, M. R.; Boddeda, A.; Timerghazin, Q. K.; Rathore, R. Key Role of End-capping Groups in Optoelectronic Properties of Poly-p-phenylene Cation Radicals. *J. Phys. Chem. C.* **2014**, *118*, 21400-21408.
(14) Cohen, A. J.; Mori-Sánchez, P.; Yang, W. Challenges for Density Functional Theory. *Chem. Rev.* **2011**, *112*, 289-320.

(15) Cohen, A. J.; Mori-Sánchez, P.; Yang, W. Insights Into Current Limitations of Density Functional Theory. *Science.* **2008**, *321*, 792-794.
(16) Frisch, M. J.; Trucks, G. W.; Schlegel, H. B.; Scuseria, G. E.; Robb, M. A.; Cheeseman, J. R.; Scalmani, G.; Barone, V.; Mennucci, B.; Petersson, G. A.; Nakatsuji, H.; Caricato, M.; Li, X.; Hratchian, H. P.; Izmaylov, A. F.; Bloino, J.; Zheng, G.; Sonnenberg, J. L.; Hada, M.; Ehara, M.; Toyota, K.; Fukuda, R.; Hasegawa, J.; Ishida, M.; Nakajima, T.; Honda, Y.; Kitao, O.; Nakai, H.; Vreven, T.; Montgomery, J. A.; Peralta, J. E.; Ogliaro, F.; Bearpark, M.; Heyd, J. J.; Brothers, E.; Kudin, K. N.; Staroverov, V. N.; Kobayashi, R.; Normand, J.; Raghavachari, K.; Rendell, A.; Burant, J. C.; Iyengar, S. S.; Tomasi, J.; Cossi, M.; Rega, N.; Millam, J. M.; Klene, M.; Knox, J. E.; Cross, J. B.; Bakken, V.; Adamo, C.; Jaramillo, J.; Gomperts, R.; Stratmann, R. E.; Yazyev, O.; Austin, A. J.; Cammi, R.; Pomelli, C.; Ochterski, J. W.; Martin, R. L.; Morokuma, K.; Zakrzewski, V. G.; Voth, G. A.; Salvador, P.; Dannenberg, J. J.; Dapprich, S.; Daniels, A. D.; Farkas; Foresman, J. B.; Ortiz, J. V.; Cioslowski, J.; Fox, D. J. Gaussian, Inc., Wallingford CT, 2009.
(17) Tomasi, J.; Mennucci, B.; Cammi, R. Quantum Mechanical Continuum Solvation Models. *Chem. Rev.* **2005**, *105*, 2999-3094.
(18) Miertu\vs, S.; Scrocco, E.; Tomasi, J. Electrostatic Interaction of a Solute with a Continuum. A Direct Utilizaion of AB Initio Molecular Potentials for the Prevision of Solvent Effects. *Chem. Phys.* **1981**, *55*, 117-129.
(19) Cossi, M.; Barone, V.; Mennucci, B.; Tomasi, J. Ab Initio Study of Ionic Solutions by a Polarizable Continuum Dielectric Model. *Chem. Phys. Lett.* **1998**, *286*, 253-260.
(20) Cances, E.; Mennucci, B.; Tomasi, J. A New Integral Equation Formalism for the Polarizable Continuum Model: Theoretical Background and Applications to Isotropic and Anisotropic Dielectrics. *J. Chem. Phys.* **1997**, *107*, 3032-3041.
(21) Ribeiro, R. F.; Marenich, A. V.; Cramer, C. J.; Truhlar, D. G. Use of Solution-phase Vibrational Frequencies in Continuum Models for the Free Energy of Solvation. *J. Phys. Chem. B.* **2011**, *115*, 14556-14562.
(22) Fukui, K. The Path of Chemical Reactions-the IRC Approach. *Acc. Chem. Res.* **1981**, *14*, 363-368.
(23) Bauernschmitt, R.; Ahlrichs, R. Stability Analysis for Solutions of the Closed Shell Kohn--Sham Equation. *J. Chem. Phys.* **1996**, *104*, 9047-9052.
(24) Weinhold, F.; Landis, C. R. *Valency and bonding: a natural bond orbital donor-acceptor perspective*; Cambridge University Press: 2005.
(25) Reed, A. E.; Weinstock, R. B.; Weinhold, F. Natural Population Analysis. *J. Chem. Phys.* **1985**, *83*, 735-746.
(26) Cossi, M.; Barone, V. Time-dependent Density Functional Theory for Molecules in Liquid Solutions. *J. Chem. Phys.* **2001**, *115*, 4708-4717.
(27) Cammi, R.; Mennucci, B.; Tomasi, J. Fast Evaluation of Geometries and Properties of Excited Molecules in Solution: A Tamm-Dancoff Model with Application to 4-dimethylaminobenzonitrile. *J. Phys. Chem. A.* **2000**, *104*, 5631-5637.
(28) Stratmann, R. E.; Scuseria, G. E.; Frisch, M. J. An Efficient Implementation of Time-dependent Density-functional Theory for the Calculation of Excitation Energies of Large Molecules. *J. Chem. Phys.* **1998**, *109*, 8218-8224.
(29) Casida, M. E.; Jamorski, C.; Casida, K. C.; Salahub, D. R. Molecular Excitation Energies to High-lying Bound States From Time-dependent Density-functional

Response Theory: Characterization and Correction of the Time-dependent Local Density Approximation Ionization Threshold. *J. Chem. Phys.* **1998**, *108*, 4439-4449.
(30) Bauernschmitt, R.; Ahlrichs, R. Treatment of Electronic Excitations Within the Adiabatic Approximation of Time Dependent Density Functional Theory. *Chem. Phys. Lett.* **1996**, *256*, 454-464.
(31) Banerjee, M.; Vyas, V. S.; Lindeman, S. V.; Rathore, R. Isolation and X-ray Structural Characterization of Tetraisopropylpyrene Cation Radical. *Chem. Commun. (Camb).* **2008**, 1889-1891.
(32) Talipov, M. R.; Navale, T. S.; Hossain, M. M.; Shukla, R.; Ivanov, M. V.; Rathore, R. Dihedral Angle-Controlled Crossover From Static Hole Delocalization to Dynamic Hopping in Biaryl Cation Radicals. *Angew. Chem. Int. Ed.* **2017**, *129*, 272-275.
(33) Brunschwig, B. S.; Creutz, C.; Sutin, N. Optical Transitions of Symmetrical Mixed-valence Systems in the Class II--III Transition Regime. *Chem. Soc. Rev.* **2002**, *31*, 168-184.
(34) Talipov, M. R.; Ivanov, M. V.; Rathore, R. Inclusion of Asymptotic Dependence of Reorganization Energy in the Modified Marcus-Based Multistate Model Accurately Predicts Hole Distribution in Poly-p-phenylene Wires. *J. Phys. Chem. C.* **2016**, *120*, 6402-6408.